AD-A179 301

DTIC FILE COPY

Department of Mechanical Engineering

University of Washington
Seattle, Washington 98195

CONTINUING EXPERIMENTAL STUDIES OF THE HYDRODYNAMIC CHARACTERISTICS OF BLUFF SYMMETRICAL FAIRING SECTIONS

D.E. Calkins
Associate Professor
M.A. Wyszkowski
Research Assistant

October 1986

DTIC
ELECTE
APR 2 1 1987
S D
D

DISTRIBUTION STATEMENT A
Approved for public release
Distribution Unlimited

87 4 15 121

CONTINUING EXPERIMENTAL STUDIES OF THE HYDRODYNAMIC CHARACTERISTICS OF BLUFF SYMMETRICAL FAIRING SECTIONS

D.E. Calkins
Associate Professor
M.A. Wyszkowski
Research Assistant

October 1986

DTIC
ELECTE
APR 21 1987
S D
D

ONR Contract No. N00014-85-K-0094

General Hydromechanics Research Program
Naval Sea Systems Center
Admin: D.W. Taylor Naval Ship
Research and Development Center

University of Washington
Ocean Engineering Program
Dept. of Mechanical Engineering
Seattle, Washington

DISTRIBUTION STATEMENT A
Approved for public release;
Distribution Unlimited

UNCLASSIFIED

SECURITY CLASSIFICATION OF THIS PAGE

ADA179301

REPORT DOCUMENTATION PAGE

1a REPORT SECURITY CLASSIFICATION: UNCLASSIFIED	1b RESTRICTIVE MARKINGS: N/A
2a SECURITY CLASSIFICATION AUTHORITY: N/A	3 DISTRIBUTION/AVAILABILITY OF REPORT: APPROVED FOR PUBLIC RELEASE; DISTRIBUTION UNLIMITED
2b DECLASSIFICATION/DOWNGRADING SCHEDULE: N/A	
4 PERFORMING ORGANIZATION REPORT NUMBER(S)	5 MONITORING ORGANIZATION REPORT NUMBER(S)
6a NAME OF PERFORMING ORGANIZATION: Dep't of Mechanical Engr U/Washington; 6b OFFICE SYMBOL (If applicable)	7a NAME OF MONITORING ORGANIZATION: DAVID W. TAYLOR NAVAL SHIP RESEARCH AND DEVELOPMENT CENTER, Code 1504 (1505)
6c ADDRESS (City, State, and ZIP Code): Seattle, Washington 98195	7b ADDRESS (City, State, and ZIP Code): BETHESDA, MARYLAND 20084-5000
8a NAME OF FUNDING/SPONSORING ORGANIZATION: Naval Sea Systems Command; 8b OFFICE SYMBOL (If applicable): SEA 05R24	9 PROCUREMENT INSTRUMENT IDENTIFICATION NUMBER: Contract Number - N00014-85-K-0094
8c ADDRESS (City, State, and ZIP Code): Washington, D. C. 20360	10 SOURCE OF FUNDING NUMBERS: PROGRAM ELEMENT NO 61153N; PROJECT NO SR 023 01; TASK NO 23454; WORK UNIT ACCESSION NO N/A

11 TITLE (Include Security Classification) (U) CONTINUING EXPERIMENTAL STUDIES OF THE HYDRODYNAMIC Characteristics of bluff symmetrical fairing sections

12 PERSONAL AUTHOR(S): D. E. Calkins & M. A. Wyszkowski

13a TYPE OF REPORT	13b TIME COVERED	14 DATE OF REPORT (Year, Month, Day)	15 PAGE COUNT
Final	FROM _____ TO _____	Oct 1986	73

16 SUPPLEMENTARY NOTATION: Sponsored under the Naval Sea Systems Command General Hydromechanics Research (GHR) Program administered by the David W. Taylor Naval Ship R&D Center, Code 1504(1505), Bethesda, Maryland 20084-5000

17 COSATI CODES			18 SUBJECT TERMS (Continue on reverse if necessary and identify by block number)
FIELD	GROUP	SUB-GROUP	(U) GHR Program (Bluff Bodies)
20	04		

19 ABSTRACT (Continue on reverse if necessary and identify by block number)

An experimental wind tunnel investigation has been conducted to determine the hydrodynamic characteristics of bluff symmetrical sections with high thickness chord ratios. The sections may be used as fairings for circular pipes, which are deeply immersed in the ocean environment so that they are cavitation free. The fairings serve to reduce drag and lateral vibrations due to vortex shedding. The sections tested were based on a family known as JFS-62M-TR mod with thickness chord ratios of 0.25, 0.30, 0.35 and 0.40. Measurements included the two dimensional profile drag coefficient, chordwise neutral stability point, and boundary layer transition and separatin locations.

20 DISTRIBUTION/AVAILABILITY OF ABSTRACT	21 ABSTRACT SECURITY CLASSIFICATION
☒ UNCLASSIFIED/UNLIMITED ☐ SAME AS RPT ☐ DTIC USERS	UNCLASSIFIED
22a NAME OF RESPONSIBLE INDIVIDUAL: Mr. V. J. Monacella	22b TELEPHONE (Include Area Code): 202-227-1503; 22c OFFICE SYMBOL: Code 1504/1505

DD FORM 1473, 84 MAR — 83 APR edition may be used until exhausted; All other editions are obsolete

SECURITY CLASSIFICATION OF THIS PAGE

UNCLASSIFIED

TABLE OF CONTENTS

Accesion For
NTIS CRA&I [X]
DTIC TAB [ ]
Unannounced [ ]
Justification
By
Distribution /
Availability Codes
Dist | Avail and / or Special
A-1

ABSTRACT

An experimental wind tunnel investigation has been conducted to determine the hydrodynamic characteristics of bluff symmetrical sections with high thickness/chord ratios. The sections may be used as fairings for circular cylindrical members, such as towing cables and offshore drilling rig riser pipes, which are deeply immersed in the ocean environment so that they are cavitation free. The fairings serve to reduce drag and lateral vibrations due to vortex shedding. The sections tested were based on a family known as JFS-62M-TR mod with thickness/chord ratios of 0.25, 0.30, 0.35 and 0.40. Measurements included the two-dimensional profile drag coefficient, chordwise neutral stability point, and boundary layer transition and separation locations.

ADMINISTRATIVE INFORMATION

This research was carried out under the Naval Sea Systems Command General Hydromechanics Research Program administered by the David W. Taylor Naval Ship Research and Development Center, under Office of Naval Research Contract No. N00014-85-K-0094.

1.0 INTRODUCTION

Marine applications of line (high length/diameter ratio) structures with circular cylindrical sections include moored and towed cable systems and risers for offshore drilling rigs. All of these systems experience relative motion between the line structure and the surrounding water, due either to ship motion or current and wave motion. Because of this relative motion, the line structure experiences unsteady (time-dependent) hydrodynamic forces due to vortex shedding. When the frequency of the vortex shedding is close to the natural frequency of the line structure, a resonant structural response condition will occur. This resonant condition will increase the drag force (force parallel to current field) which in turn will result in cyclic motions and stresses.

One solution to the shed vortex problem is to fair the circular cylinder with a streamlined shape. An obvious drawback is that the fairing, unless it is allowed to swivel freely and align itself with the flow field, will act as a wing and generate large transverse lift forces. However, this in turn dictates that the position of the hydrodynamic (aerodynamic) center must be aft of the mechanical center of rotation (central axis of the line structure) for weathervane stability.

It should be noted that the hydrodynamic center, or neutral stability point, is used in contrast to the center of pressure. The hydrodynamic center is defined as the position along the chord about which the moment coefficient is constant independent of lift coefficient, while the center of pressure position varies with lift coefficient. For symmetrical sections, this constant moment coefficient has a value of zero. The neutral point is defined as the point along the chord where the slope of pitching moment coefficient versus lift coefficient curve is zero. Therefore the terms hydrodynamic center and neutral point are synonymous for a symmetrical section, and are used interchangeably.

The selection of an optimum airfoil section shape for use as a fairing must include consideration of the following:

(1) streamlined symmetrical section for low drag
(2) position of maximum thickness/chord as close to the leading edge as possible in order for center of rotation to be forward of hydrodynamic center for weathervane stability
(3) high thickness/chord ratio (bluff) sections to reduce the chord size of the fairings
(4) separation free boundary layer

The utilization of bluff sections as fairings will lead to problems with boundary layer separation. Some means must therefore be used to prevent or control boundary leyer separation and to provide rotational stability. The use of separation resistant sections has been evaluated, Calkins and Gray [1], as a solution to this problem. Five sections were evaluated during the Phase 1 study, Fig. 1.1:

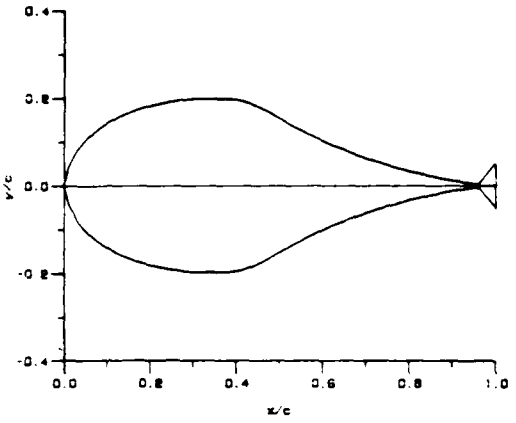

Liebeck 40% Section Profile with Trailing Edge Wedge

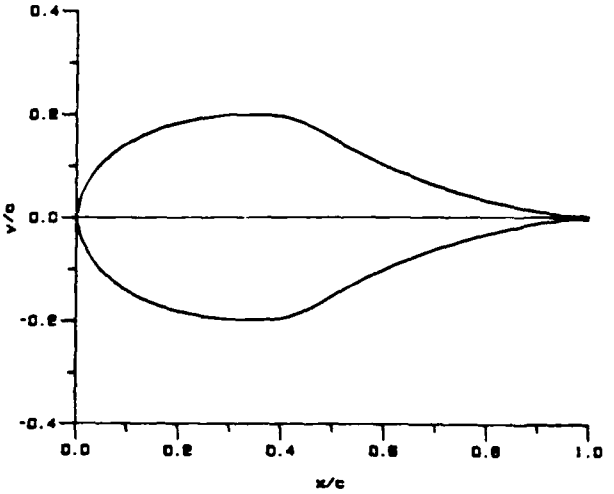

Liebeck 40% Section Profile

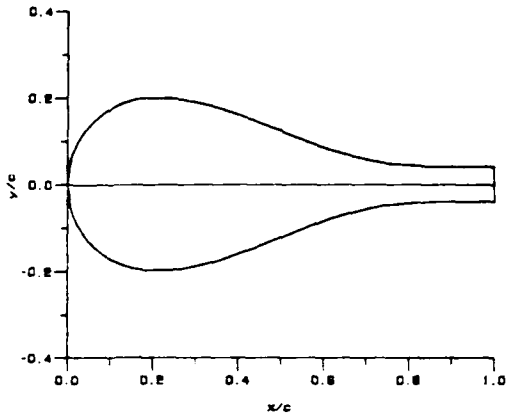

JfS 61M-TR-40 Section Profile

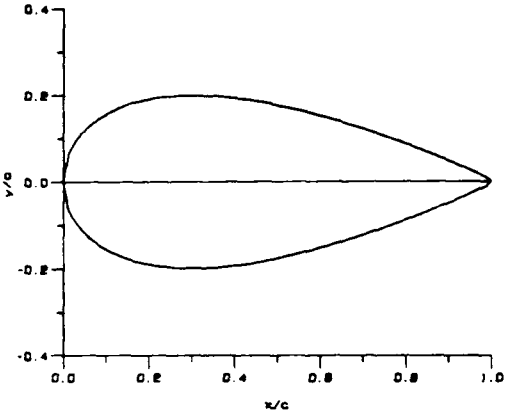

NACA 0040 Section Profile

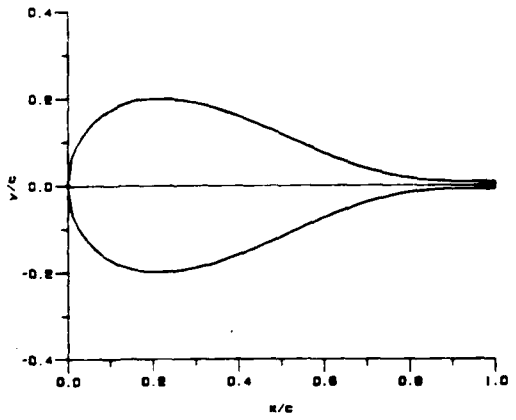

JfS 62M-TR-40 Section Profile

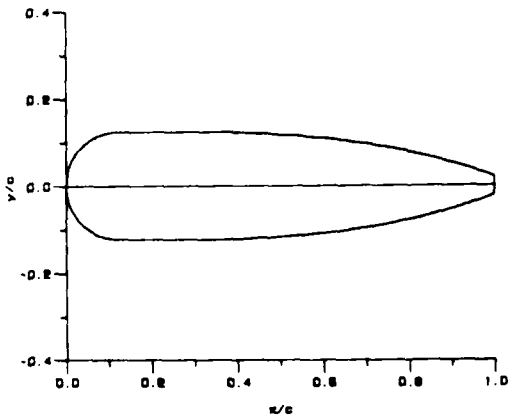

Fathom Flexnose 25% Section Profile

Fig. 1.1 Fairing sections

Section	t/c	x_t/c	r/c	Pressure recovery section shape
Fathom	0.25	0.125	0.125	Convex
NACA 0040	0.40	0.30	0.125	Convex
Liebeck	0.40	0.35	0.1763	Concave
Jfs 61-TR-40	0.40	0.20	0.25	Concave
Jfs 62-TR-40	0.40	0.20	0.25	Concave

The aerodynamic characteristics of the sections were evaluated and compared on the basis of:

1) Boundary Layer Characteristics
2) Profile Drag Coefficient
3) Hydrodynamic Center Locations

In evaluating the hydrodynamic characteristics of the five fairings it was evident that the JfS 62M-TR-40 section best met the performance criteria. The boundary layer for this section was well behaved, and separation was a problem only at Reynolds numbers less than $.25 \times 10^5$. Its hydrodynamic center was well aft since the restoring moment gradient was high. The drag coefficients, although higher than those of the NACA and Liebeck section, were within the range predicted by Hoerner [2] for other sections of comparable thickness. The JfS 62M section with its thin trailing edge has lower drag coefficients than the JfS 61M section. The JfS 61M section was in every other way comparable to the JfS 62M.

2.0 PHASE (2) OBJECTIVES

The objective of the Phase (2) research was to continue the experimental investigation of the hydrodynamic characteristics of the JFS 62-TR blurr symmetrical fairing section. The JFS mod section served as a parent for a thickness/chord ratio (t/c) family of 0.25, 0.3, 0.35 and 0.4.

Phase (2) tests continued the 2-dimensional characterization of the fairing section in the UW "Venturi" tunnel by measuring the lift, drag and pitching moments using the 3-component balance with the model mounted horizontally between two vertical end plates. The goal was to determine the 2-dimensional lift and pitching moment characteristics, which were not determined in the Phase (1) tests, and to determine the drag coefficient, which would then be used to check the wake measurement technique. The free rotation tests were also repeated to determine the hydrodynamic center position.

3.0 SYMMETRICAL FAIRING SECTION MODELS

3.1 JFS Section

The JFS sections, Thieme [3], are members of a family of balanced ship rudder profiles developed at the Shipbuilding Institute of the University of Hamburg. These profiles were developed by a systematic variation of eight form parameters which included:

1) cross-sectional area,
2) leading edge radius of curvature, (r_n)
3) length of forebody, (n)
4) length of pressure recovery section, (p)
5) length of trailing edge, (g)
6) thickness of trailing edge, (t_{te})
7) surface slopes, and
8) radius of curvature at maximum thickness. (r_b)

The profile coordinates are expressed as polynomials composed of so-called influence functions. One influence function was written for each of the form parameters.

3.2 Section Geometry

The primary parameters for the section geometry are the following, Fig. 3.1.

(1) maximum thickness/chord ratio (t/c)
(2) chordwise position of maximum thickness ($x_{t/c}$)
(3) nose radius of curvature (r/c)
(4) trailing edge thickness ($t_{e/c}$).

In addition, the shape of the section aft of the maximum thickness location may be described as either concave or convex. The JFS 62-TR section was modified by reshaping the leading edge radius to a forebody which was circular in section to the maximum thickness position.

An important geometrical consideration for a symmetrical section designed to fair a circular cylindrical cable is that the circular diameter be inscribed in the fairing as far forward as possible. Fig. 3.2 shows the nondimensional diameter, d/c, of these circles as a function of chord location. The center of each circle corresponds to the mechanical pivot location of the fairing.

An important geometrical characteristic of the fairing shape is the local surface angle. Since the pressure gradient is a function of this angle, the surface slope for the Jfs 62M TR-40 section as a function of the chord is shown in Fig. 3.3. Also indicated are the trailing edge surface angle, θ_{t_e}. Note that the JFS section has a concave pressure recovery section.

The section coordinate for the JFS 62M-TR-40 were transformed to the lower thickness/chord-ratios by direct scaling.

$$[y/c]_{t/c} = [y/c]_{40} * [t/c \,/ 0.40] \qquad (3.1)$$

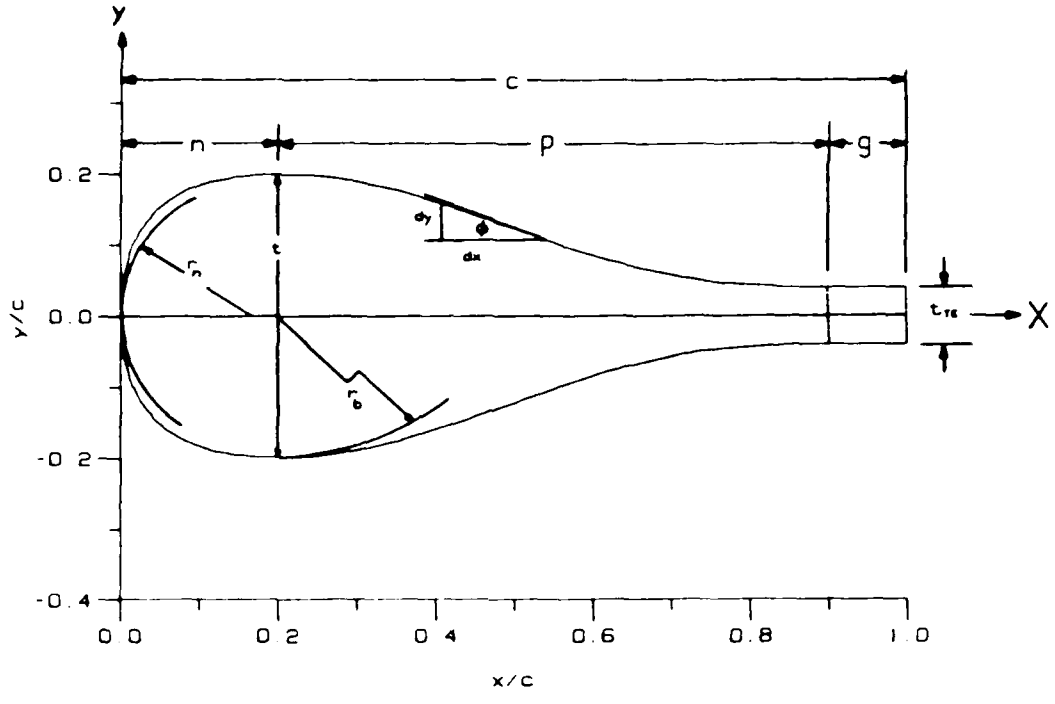

Fig. 3.1 Definition of geometric variables

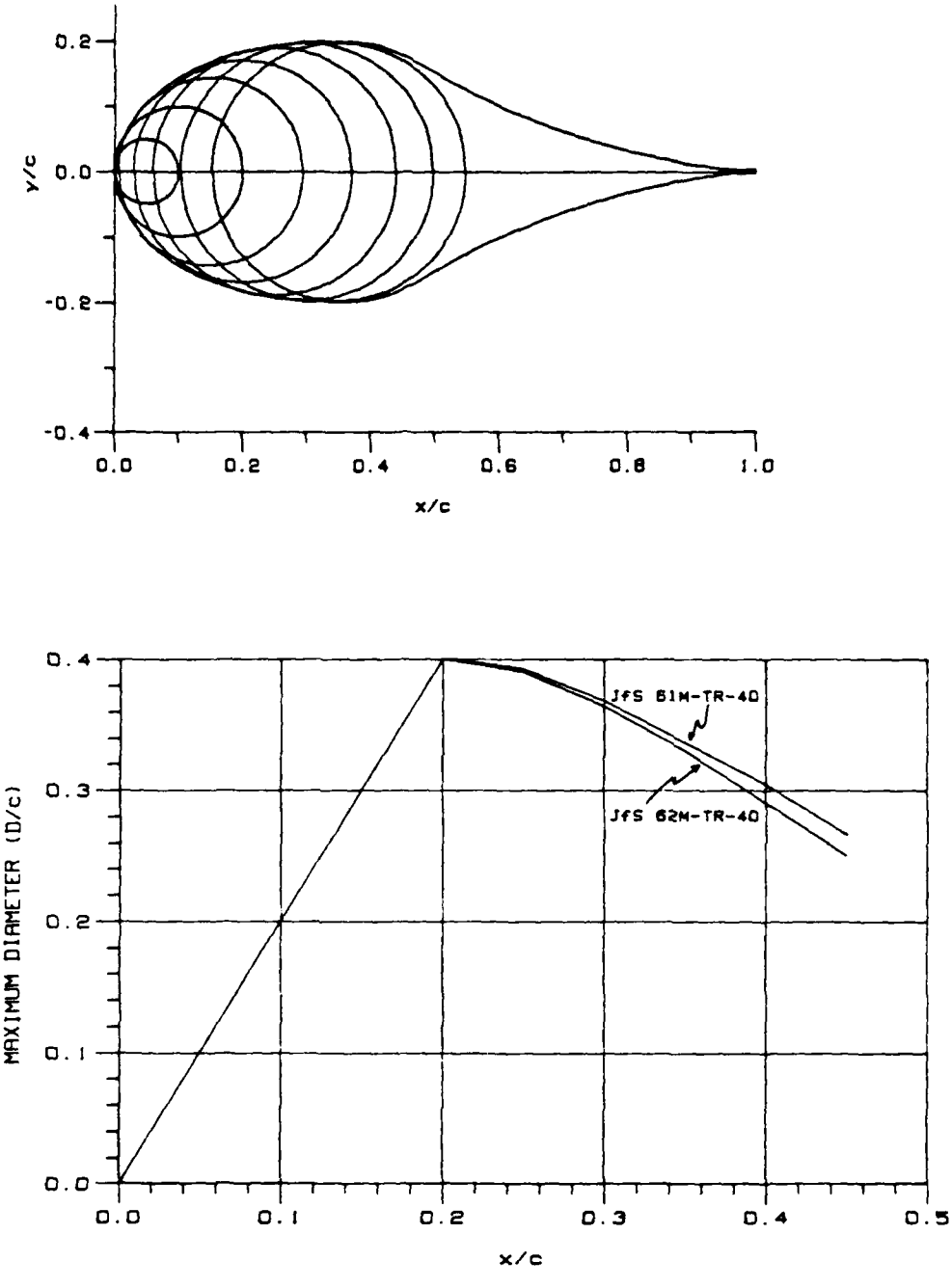

Fig. 3.2 Diameter of inscribed circles as a function of chord position for JfS modified sections

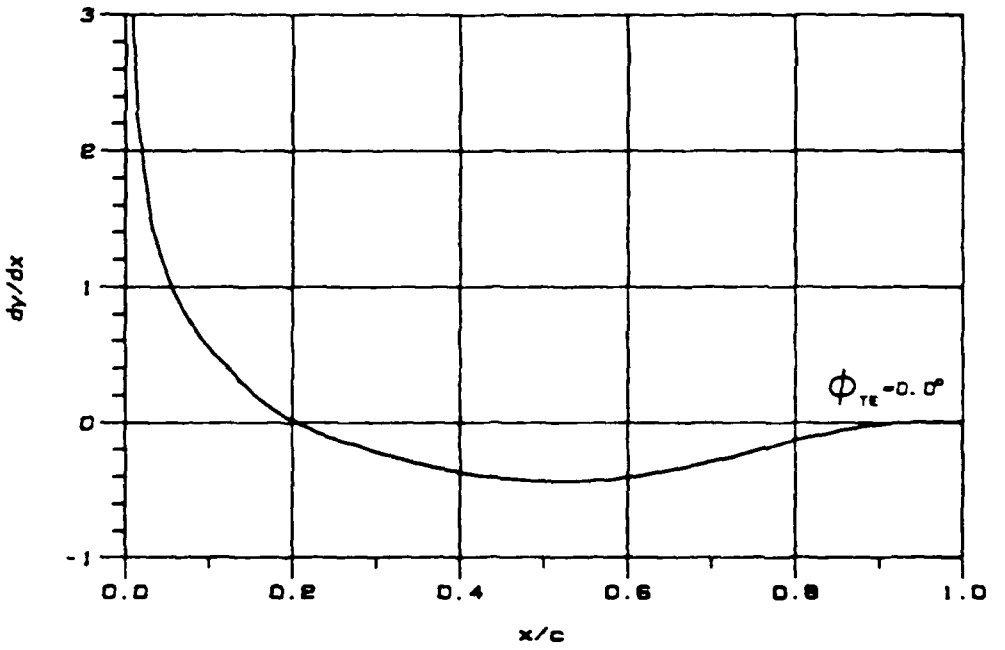

Fig. 3.3 Surface slope curve for JfS 62M-TR-40 section

The section surface coordinates are tabulated in Table 3.1, and the section shapes are shown in Fig. 3.4.

Table 3.1. JFS Fairing Section Non-dimensional Surface Coordinates

	+y/c			
	Jfs 62M TR-25	Jfs 62M TR-30	Jfs 62M TR-35	Jfs 62M TR-40
x/c	t/c 0.25	0.30	0.35	0.40
0.000	0.00000	0.00000	0.00000	0.00000
0.004	0.02488	0.02985	0.03483	0.03980
0.010	0.03903	0.04684	0.05464	0.06245
0.020	0.05449	0.06539	0.07628	0.08718
0.040	0.07500	0.09000	0.10500	0.12000
0.060	0.08927	0.10712	0.12498	0.14283
0.080	0.10000	0.12000	0.14000	0.16000
0.120	0.11456	0.13748	0.16039	0.18330
0.125	0.11588	0.13905	0.16223	0.18540
0.160	0.12248	0.14697	0.17147	0.19596
0.200	0.12500	0.15000	0.17500	0.20000
0.275	0.12113	0.14536	0.16958	0.19381
0.350	0.11004	0.13205	0.15406	0.17607
0.425	0.09332	0.11198	0.13065	0.14931
0.500	0.07331	0.08798	0.10264	0.11730
0.575	0.05266	0.06319	0.07372	0.08425
0.650	0.03388	0.04066	0.04743	0.05421
0.725	0.01915	0.02298	0.02681	0.03064
0.800	0.00966	0.01160	0.01353	0.01546
0.875	0.00540	0.00648	0.00756	0.00864
0.950	0.00469	0.00563	0.00656	0.00750
1.000	0.00469	0.00563	0.00656	0.00750

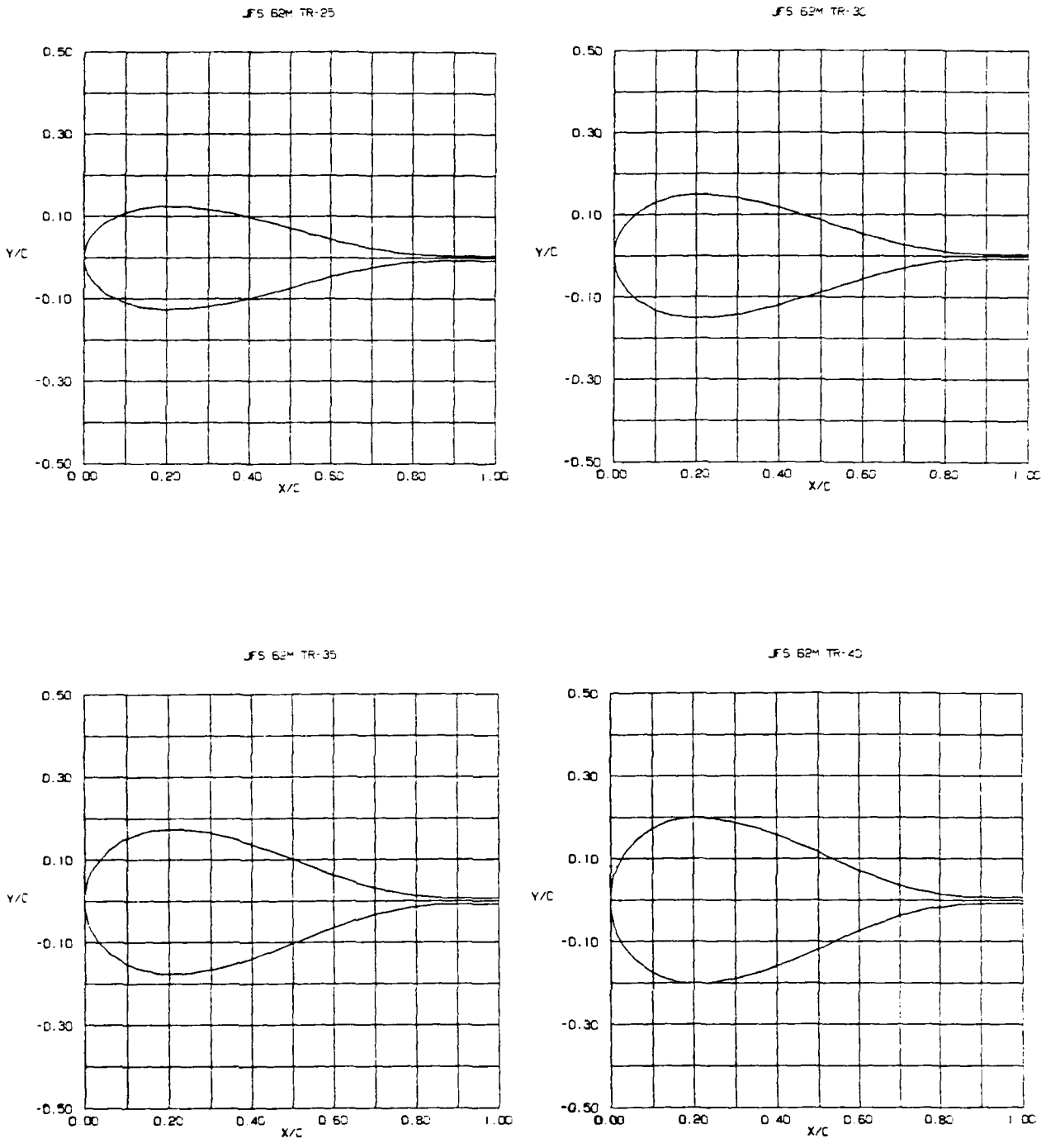

Fig. 3.4 JfS 62M-TR-thickness/chord ratio family

3.3 Wind Tunnel Model Construction

Seven models were made for the Phase (2) investigation: three 77.5 cm (30.5 in) length vertically oriented models and four 38 cm (15 in) horizontally oriented models. The fourth 77.5 cm vertical model, the JFS 62M TR-40, was available from the previous Phase (1) research. Each model had a chord length, c, of 30.5 cm (12 in) with the location of maximum thickness at the 20 percent chord position.

Each model consisted of a mahogany frame with 1/16-in birch endplates that defined the sectional shape, Fig. 3.5. The trailing edge was made from a solid mahogany plank milled to the contour of the body, Fig. 3.6. A 1/32-in birch plywood sheet was wrapped around the frame to provide a smooth, rigid skin, Fig. 3.7. Polyurethane foam was injected into the skeleton to provide structural support for the skin between frame elements. Two layers of 3/4 oz. weight fiberglass cloth were placed over the plywood to provide skin strength and smoothness. The thin trailing edge of the JFS sections was reinforced with an extra layer of fiberglass cloth to prevent warping.

Depressions in the model surface were filled with automotive body filler and smoothed using a plexiglass template. The dimensionally accurate surface was wet-sanded, coated with primer and painted with two coats of flat white automotive lacquer. The final finish of the models was extremely smooth and free of surface irregularities, Fig. 3.8 and 3.9.

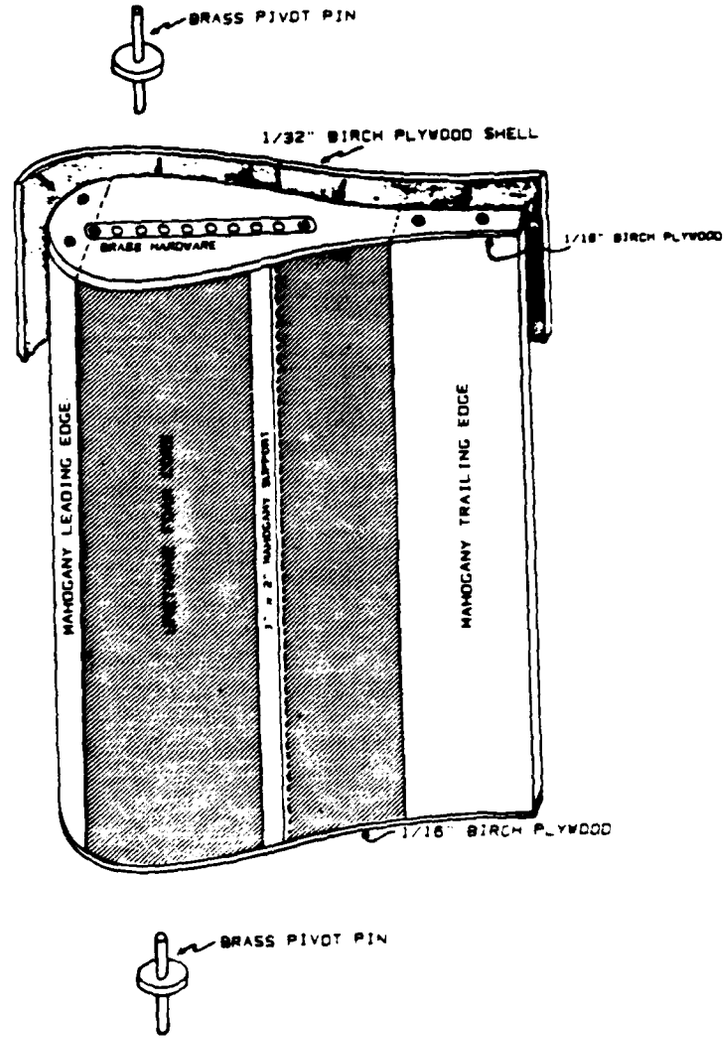

Fig. 3.5 Fairing model construction details

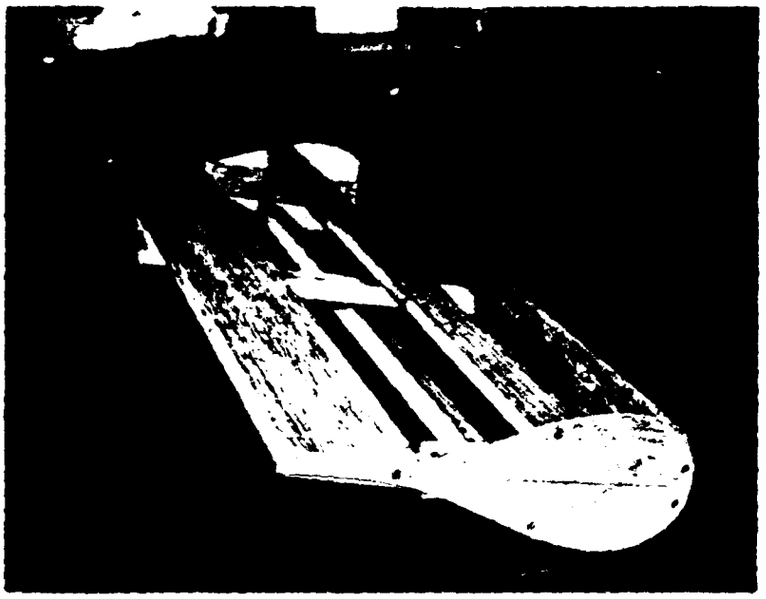

Fig. 3.6 Model interior construction

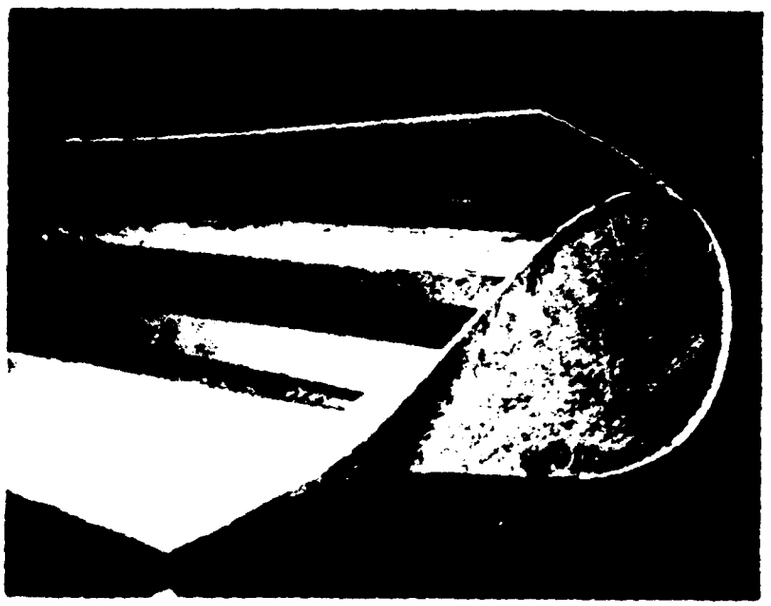

Fig. 3.7 Model plywood skin

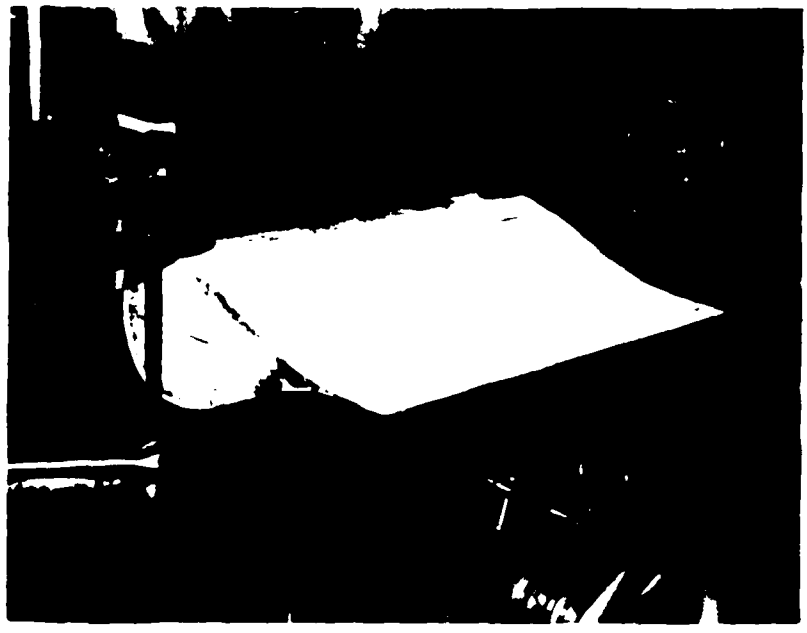

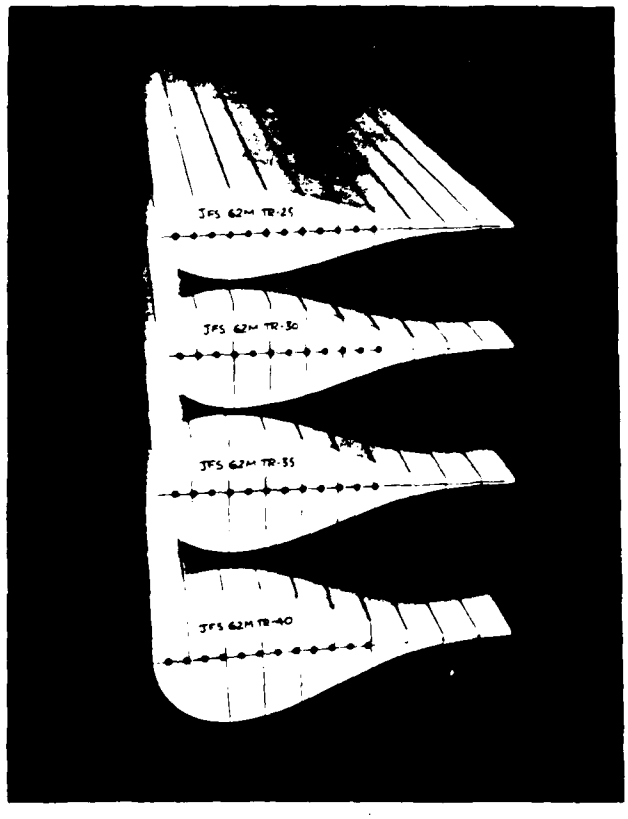

Fig. 3.8 JfS-62M fairing models

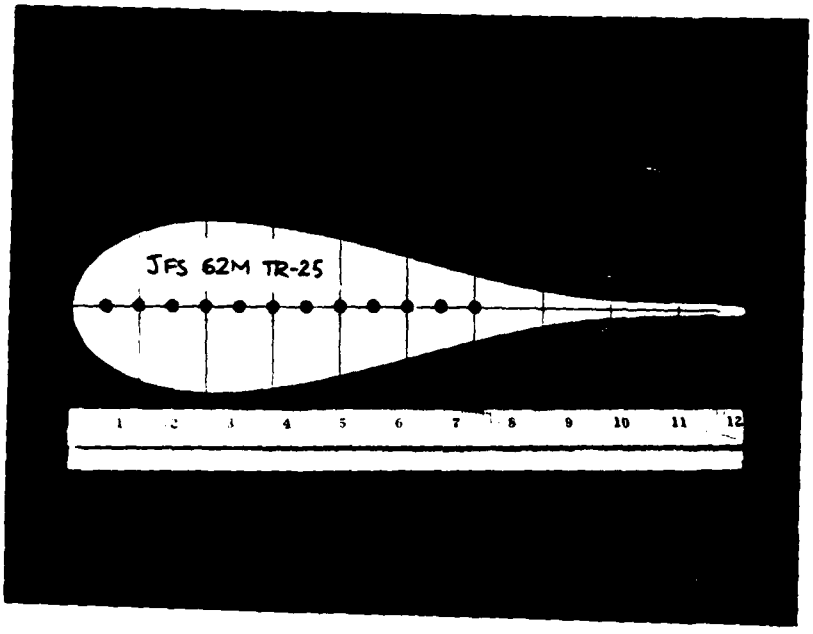

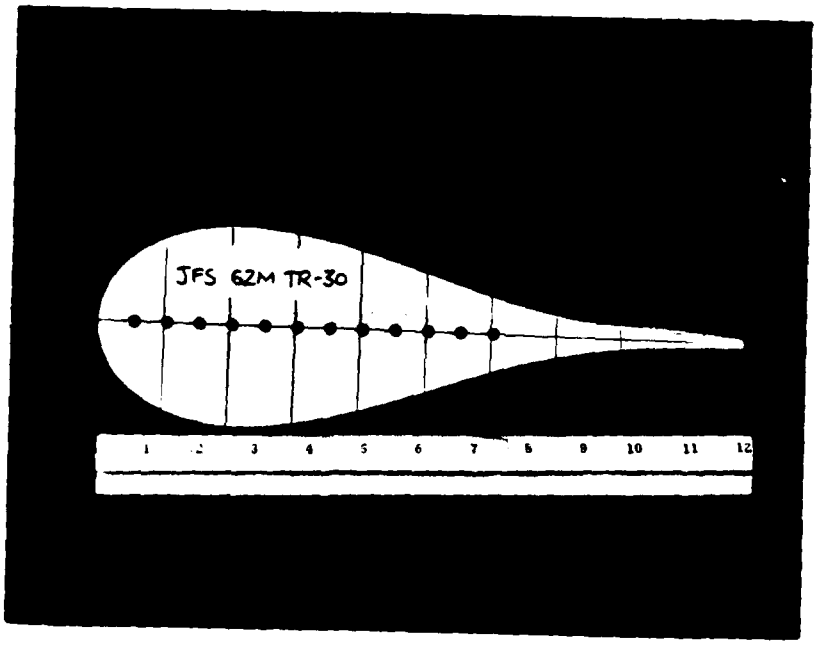

Fig. 3.9 Individual fairing section models

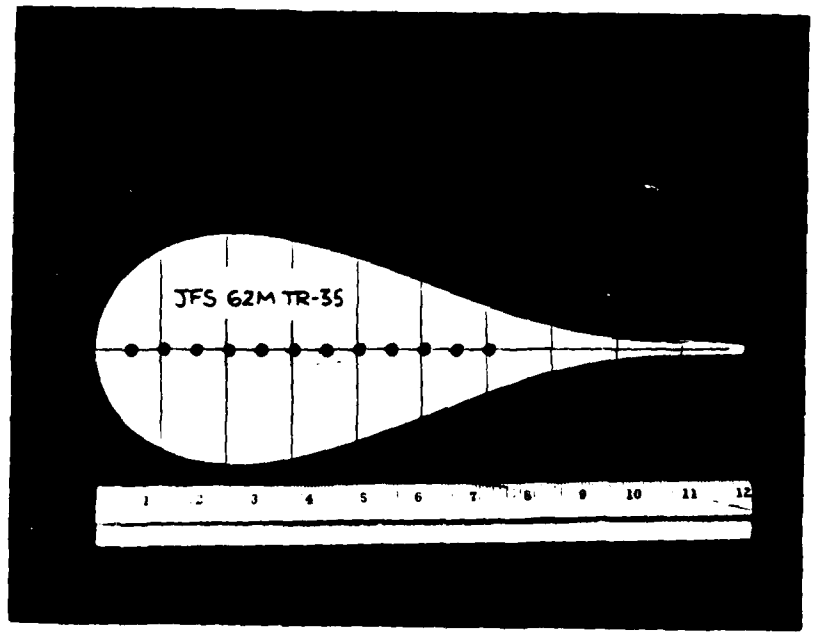

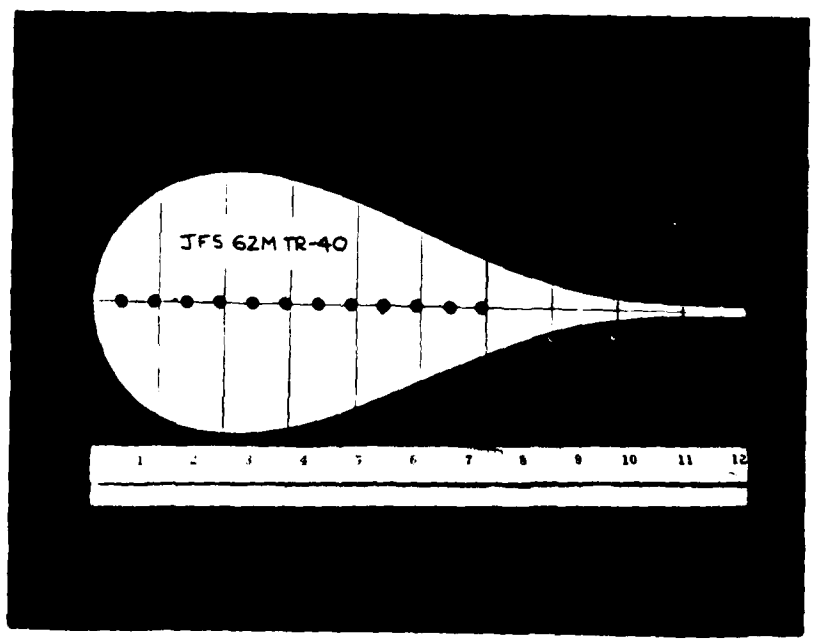

Fig. 3.9 continued

4.0 WIND TUNNEL DESCRIPTION

The use of a wind tunnel for the hydrodynamic characterization of the fairing section is appropriate, as long as Reynolds number equivalence is maintained. If it is assumed that the fairing section is being operated at depths great enough to avoid cavitation, the aerodynamic characteristics will be the same as the hydrodynamic characteristics. The tests were conducted in the University of Washington "Venturi" open return wind tunnel, which has an octagonal cross-section of 0.9 m across vertices and 0.79 m across flats. With a maximum speed of 27 m/s, a fairing section model with a 30.5 cm chord may be operated at a Reynolds number up to 5.0×10^5.

4.1 Tunnel Turbulence Intensity

The wind tunnel turbulence intensity was measured using the sphere drag coefficient method. The sphere drag coefficient was measured as a function of diameter Reynolds number. The Reynolds number at which the drag coefficient equals 0.30 is termed the "critical Reynolds number," R_{cr}. The critical Reynolds number has a value of 385,000 in free air. The turbulence factor is thus defined as

$$TF = 385{,}000./R_{cr} \tag{4.1}$$

For the Venturi Wind Tunnel:

$R_{cr} = 1.5 \times 10^5$ and $TF = 2.85$

The turbulence intensity level, T_u, is defined as

$$T_u = u/U_\infty \tag{4.2}$$

where u = root mean square (rms) velocity fluctuations

U_∞ = free stream mean velocity.

The turbulence intensity is related to the turbulence factor so that,

$T_u = 2.5$ percent

Since atmospheric turbulence levels in free flight are less than one percent, it is common to take means to reduce T_u to values below this. However, this problem must be reassessed for conditions in the ocean. In general, the turbulence intensity will vary with location and depth. An evaluation of the ocean turbulence intensity at two locations was made in Calkins and Gray [1], Fig. 4.1. The resulting turbulence intensities, for a towing speed of 5 m/s, vary between 0.09 and 0.27 percent over a depth range from 0 to 750 m in the first location, while it varies from 0.6 to 8.7 percent over a depth range from 0 to 23 m in the second location.

The wind tunnel turbulence level could have been reduced by the addition of screens at the inlet; however, this would have been at the expense of a decrease in tunnel maximum operating speed (maximum Reynolds number). Because of the wide range of variation in ocean turbulence intensity, and since maximum

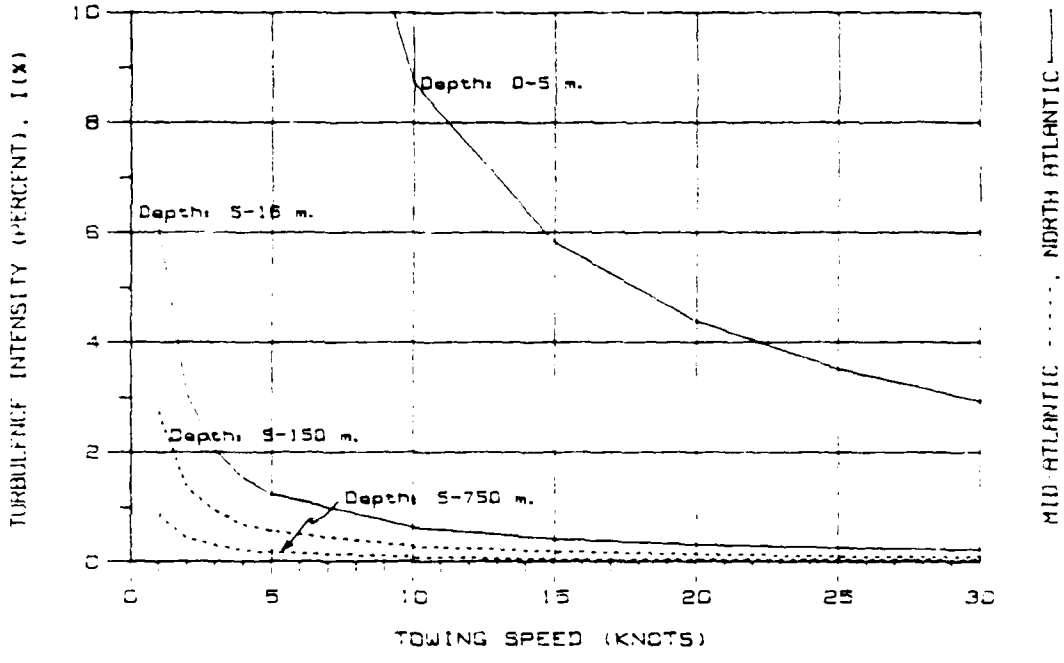

Fig. 4.1 Measured ocean turbulence intensity levels at two Atlantic Ocean locations

Reynolds number in the tunnel was considered more important, the tunnel was left in its present condition and the wind tunnel data are presented as measured.

4.2 Experimental Measurements

The following measurements were made:

(1) boundary layer visualization to determine positions of laminar to turbulent transition, and laminar or turbulent boundary layer separation.
(2) force balance measurements for profile drag coefficient
(3) wake survey to determine two-dimensional section profile drag coefficient
(4) determination of position of hydrodynamic center, or neutral stability point

4.3 Drag Coefficient

Two wind tunnel methodologies were used for determining the section profile drag coefficient. The first technique used a mechanical balance for direct measurement of the aerodynamic lift, drag, and pitching moment. The second technique is indirect. The profile drag was determined from the velocity distribution measured in the wake of the fairing.

4.3.1 Horizontally Mounted Model

The horizontally oriented models were mounted on three struts on the three component balance to provide for a ±10° variation in angle of attack, Figs. 4.2 and 4.3. A plexiglass 2-D test section was used for this investigation. The 2-D test section consisted of two 76.2 x 78.4 cm (30 x 31 in), 0.95 cm (3/8 in) thick plexiglass plates joined by four continuously threaded 0.635 cm (1/4 in) steel rods. Bolts were used to control the plate spacing and to adjust the parallelness of the plates. The leading edges of the plates were faired to reduce air flow disturbances. A 20.3 x 30.5 cm (8 x 12 in) rectangular opening in each plate provided model access while mounted on the balance, Fig. 4.4.

The model mounting system consists of two forward struts with a variable span distance to measure the lift and drag forces and a single strut aft to measure the pitching moment. The angle of attack was controlled by means of a motor driven actuating rod which was connected to the pitching moment arm. The range of the angle of attack mechanism was -12 to +12 degrees. The scale was incremented in single degree units.

All measurements were made by an automatic beam balance. Three poise motors operated on a closed loop feedback circuit to maintain the model forces in equilibrium. Each servo controled the longitudinal position of a rider on the balance lever arm which indicated the load in grams for lift and drag, and gram-centimeters for pitching moment. The maximum indicated loads were:

Lift: -300 g to 700 g
Drag: -300 g to 700 g
Pitching Moment: -600 g-cm to 400 g-cm

The indicated loads were corrected by the following relations:

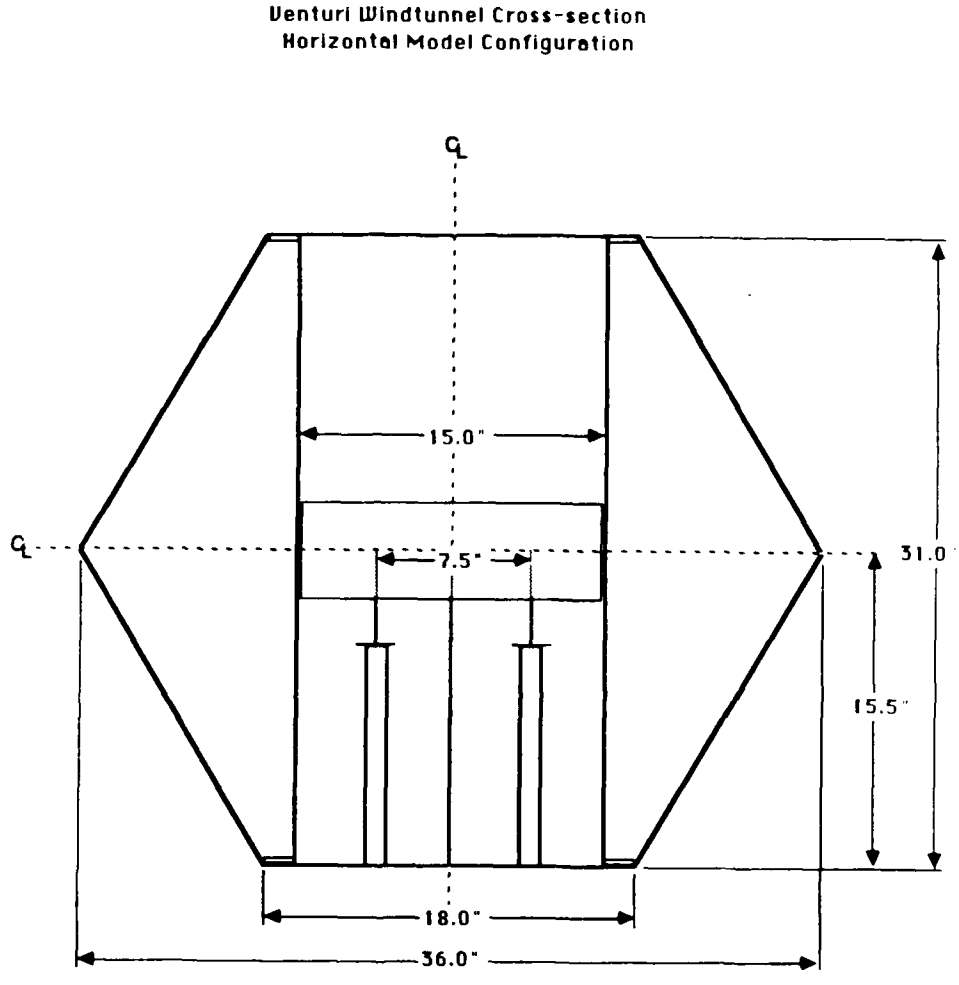

Fig. 4.2 Venturi Windtunnel cross-section - horizonal model configuration

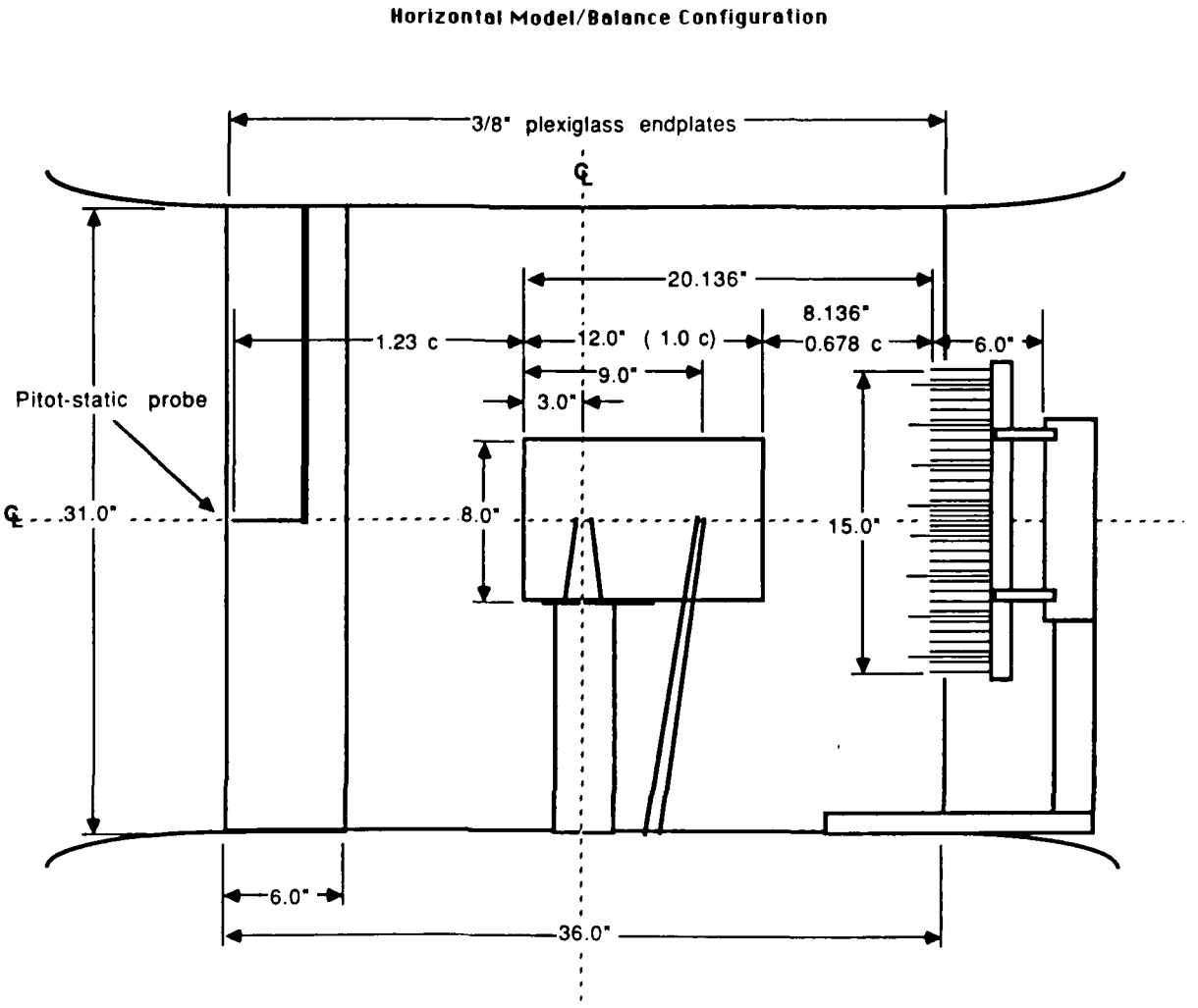

Fig. 4.3 Horizontal model/balance configuration

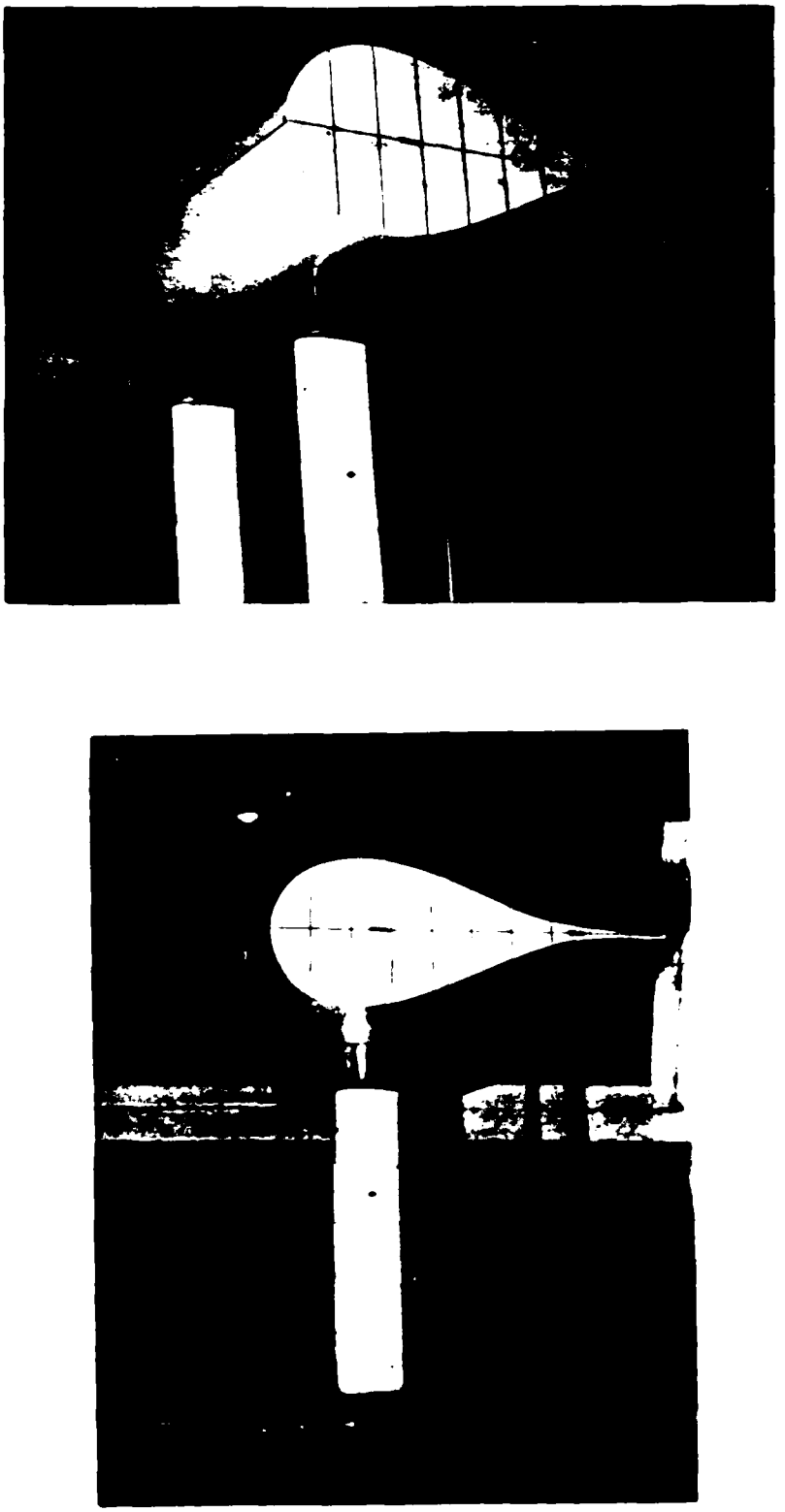

Fig. 4.4 Horizontal model/balance

$$Lr = 10*Li$$
$$Dr = 1*Di$$
$$Mr = 100*Mi \qquad (4.3)$$

4.3.2 Vertically mounted model

The two-dimensional models were mounted in a vertical position between the top and bottom of the wind tunnel, Fig. 4.5, and were free to rotate about a pivot aligned with the leading edge. The pivot position was variable along the section chord, with the center of rotation positions at five percent chord stations along the chord. Brass pivot pins, Fig. 4.6, were positioned in the top and bottom plates of the tunnel test section and were fitted into the brass plates that were recessed into the top and bottom faces of the models. A clear plexiglass plate acted as the viewing window for the wind tunnel test section. Several holes and a curved slot were cut in the plexiglass window to hold the pivot and locking pins. A protractor was etched into the plexiglass so that the yaw angle of the model could be measured. The locking pin was used to prevent the rotation of the model and to align it with the flow when the wake was being surveyed.

4.3.3 Momentum Wake Rake

The wake rake must be positioned so that the wake profile data is taken far enough downstream from the body so that the static pressure at the measuring section is equal to that in the undisturbed freestream static pressure. Pope, [4], states that locating the wake rake at least 0.7 chord behind the trailing edge of the wing is sufficient. Boulil, [5], determined that the optimum position is 0.5 chord aft of the trailing edge. Our measurements were made at 0.678 chord position.

The data for the calculation of drag by the profile method were collected by a wake rake connected to a multiple manometer board. The microcomputer based differential pressure transducer equipment used in the phase (1) test, [1], was non-functional, consequentially it was necessary to substitute the manometer board. Two rakes were used in the investigation: a horizontally oriented rake for the vertical models and a vertically oriented rake, Fig. 4.1, for simultaneous balance profile drag measurements. Both rakes used the same bank of pivot tubes.

The wake rake body consisted of 31 total head probes spaced at 1.27 cm (.5 in) intervals along the body. The center 5 probes were spaced .635 cm (.25 in) apart. The total width of the wake survey was 38.1 cm (15 in). The probes, 0.16 cm (1/16 in) OD rigid stainless steel tubing, extended 7.63 cm (3 in) from the body of the rake. Static pressure probes were made of the same tubing. These tubes extended 10.16 cm (4.0 in) from the rake body and the ends were sealed and rounded. Four 0.08 cm (1/32 in) holes were drilled perpendicular to the axis of the tubing, 2.54 cm (1 in) downstream from the leading edge. The static probes were spaced at 5.08 cm (2.0 in) intervals over the center 31.75 cm (12.5 in) of the rake. The static pressures were taken in the same plane and the same distance downstream from the model as the total head measurements.

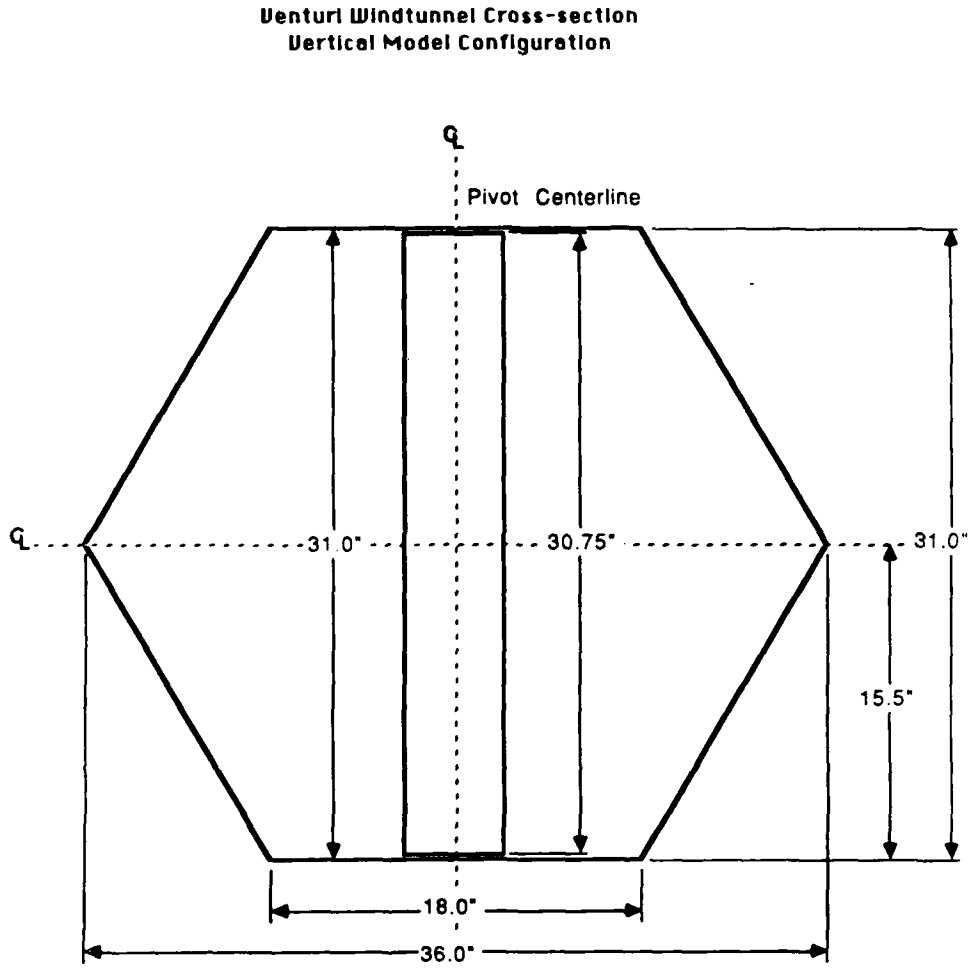

Fig. 4.5 Venturi Windtunnel cross-section - vertical model configuration

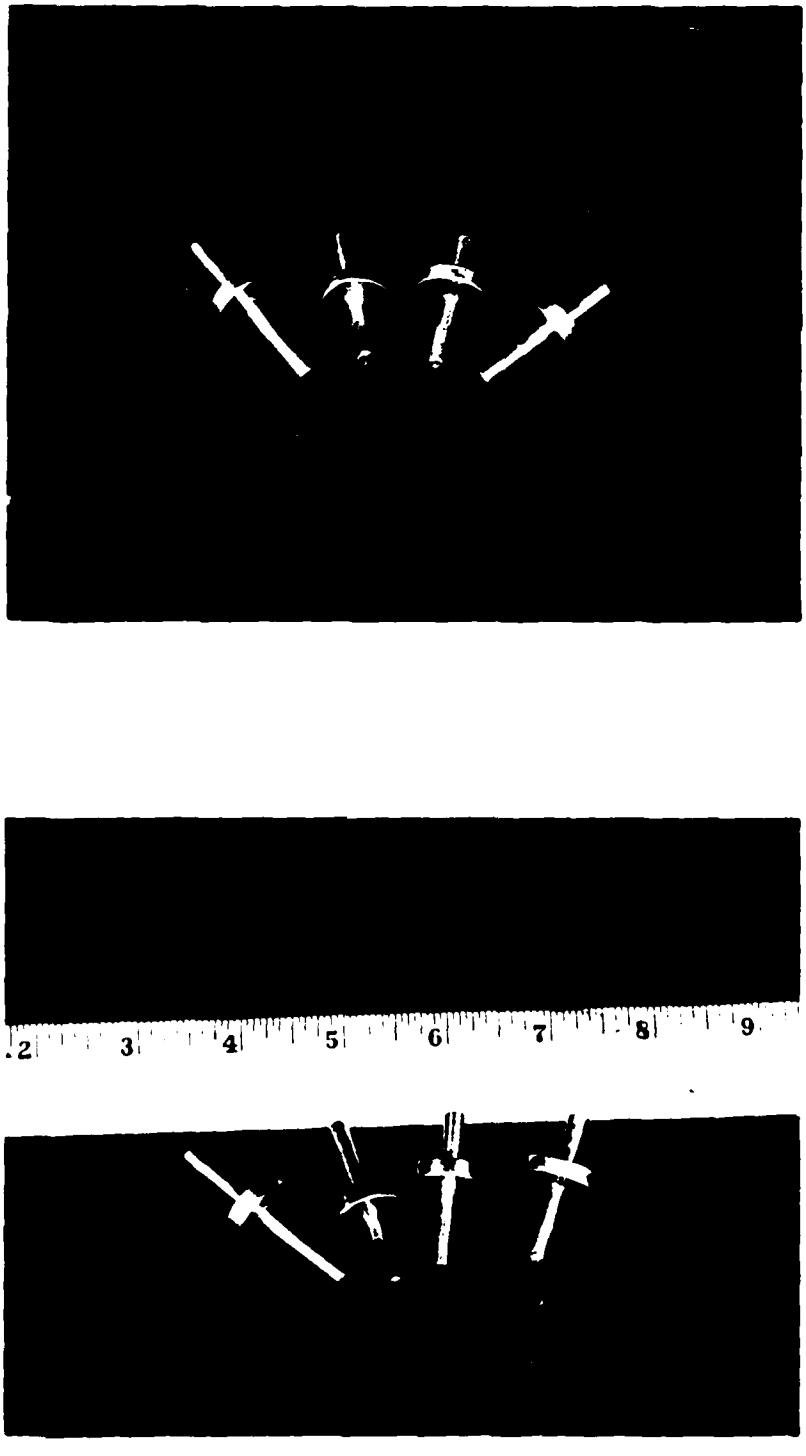

Fig. 4.6 Vertical model pivot pins

The horizontal wake rake was positioned at mid-tunnel height and 20.3 cm (8.136 in), length downstream of the model trailing edge. The wake rake was fixed in this position and was not adjustable to port or starboard. The vertical wake rake was designed to be completely adjustable in the vertical direction and somewhat adjustable either fore or aft, and port to starboard. The vertical rake was positioned in the same location as the horizontal rake, but offset 2.5 cm (1 in.) to the starboard to avoid the wake generated by the pitching moment strut.

The pitot tubes were connected to an adjustable angle, multiple manometer board by flexible, multi-coloured "strip-a-tube." The multiple manometer consisted of 25 manometer tubes supplied by a vertically adjustable reservoir of kerosene. The manometer board was tilted to 15.0° from the horizontal in order to measure low dynamic pressures. A datum line was established to account for transverse inclination in the manometer support structure and floor.

5:78

5.0 THEORETICAL ANALYSIS

A two-dimensional potential flow program (POT2D), developed by Maskew, [6], may be used to compute the pressure distribution on an arbitrary two-dimensional shape. The shape can be described either by a set of points or generated internally using an NACA four-digit airfoil section equation or the equation for an ellipse. The user can request either the lifting or non-lifting solution.

The program is based on a low-order surface singularity panel method using flat panels of constant doublet and source. The solution is nominally exact, with the accuracy improving as the number of panels is increased. The program provides the panel doublet values by simultaneously satisfying the internal Dirichlet boundary condition of zero perturbation potential at a control point under the center of each panel. The panel source values are determined directly by the external Neumann boundary condition of zero normal velocity. The surface perturbation tangential velocities are obtained from the gradient of the doublet distribution. The pressure force coefficients on the panels are then summed to provide overall force and moment values.

POT2D was used for the JFS sections with the tabular data contained in Table 3.1 as the input. The velocity ratio and the pressure coefficient distributions on the surface as a function of chord are shown in Figs. 5.1 and 5.2. POT2D was run for a non-lifting solution at 0.0° angle of attack. Each section was defined by 44 panels.

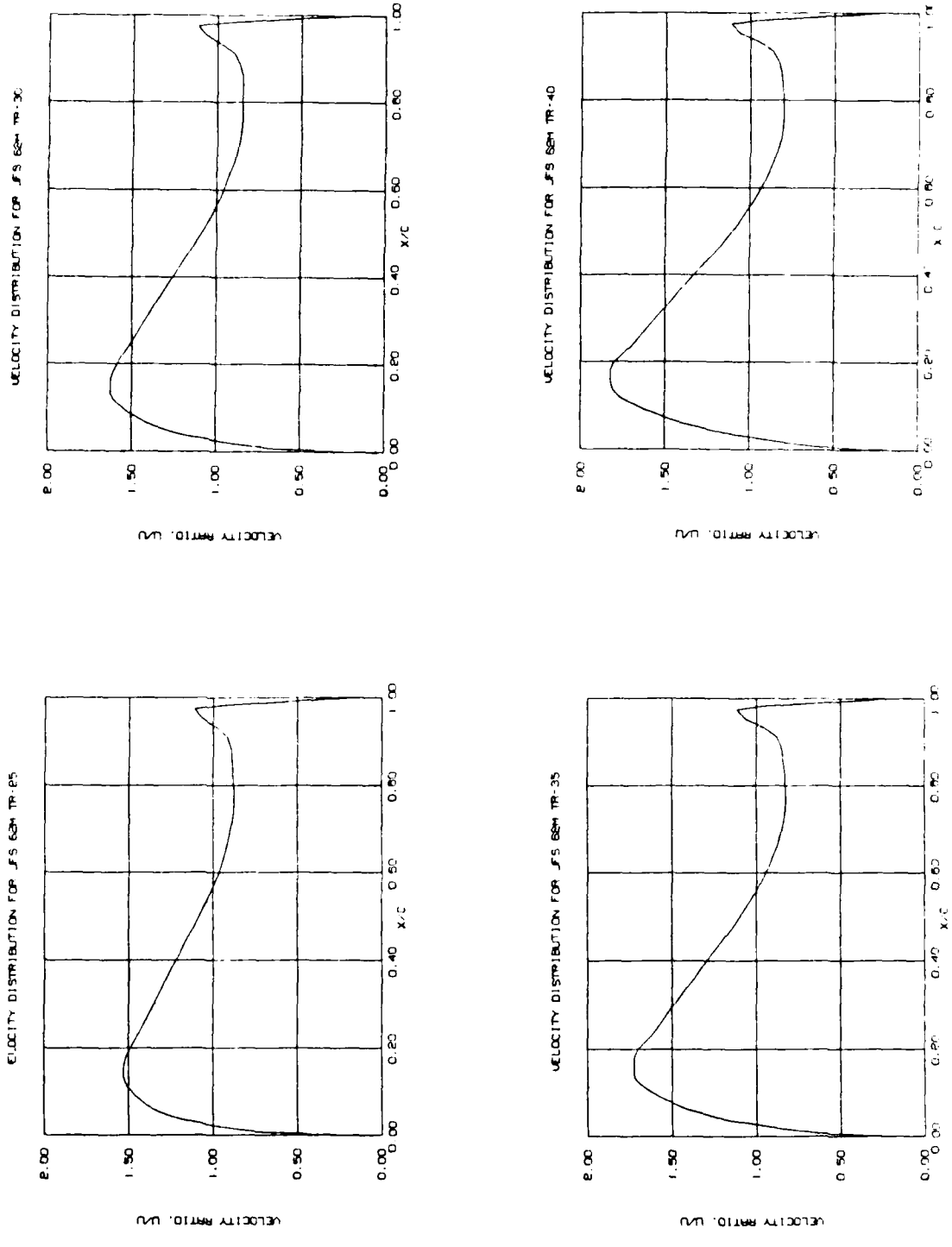

Fig. 5.1 JfS section velocity distributions

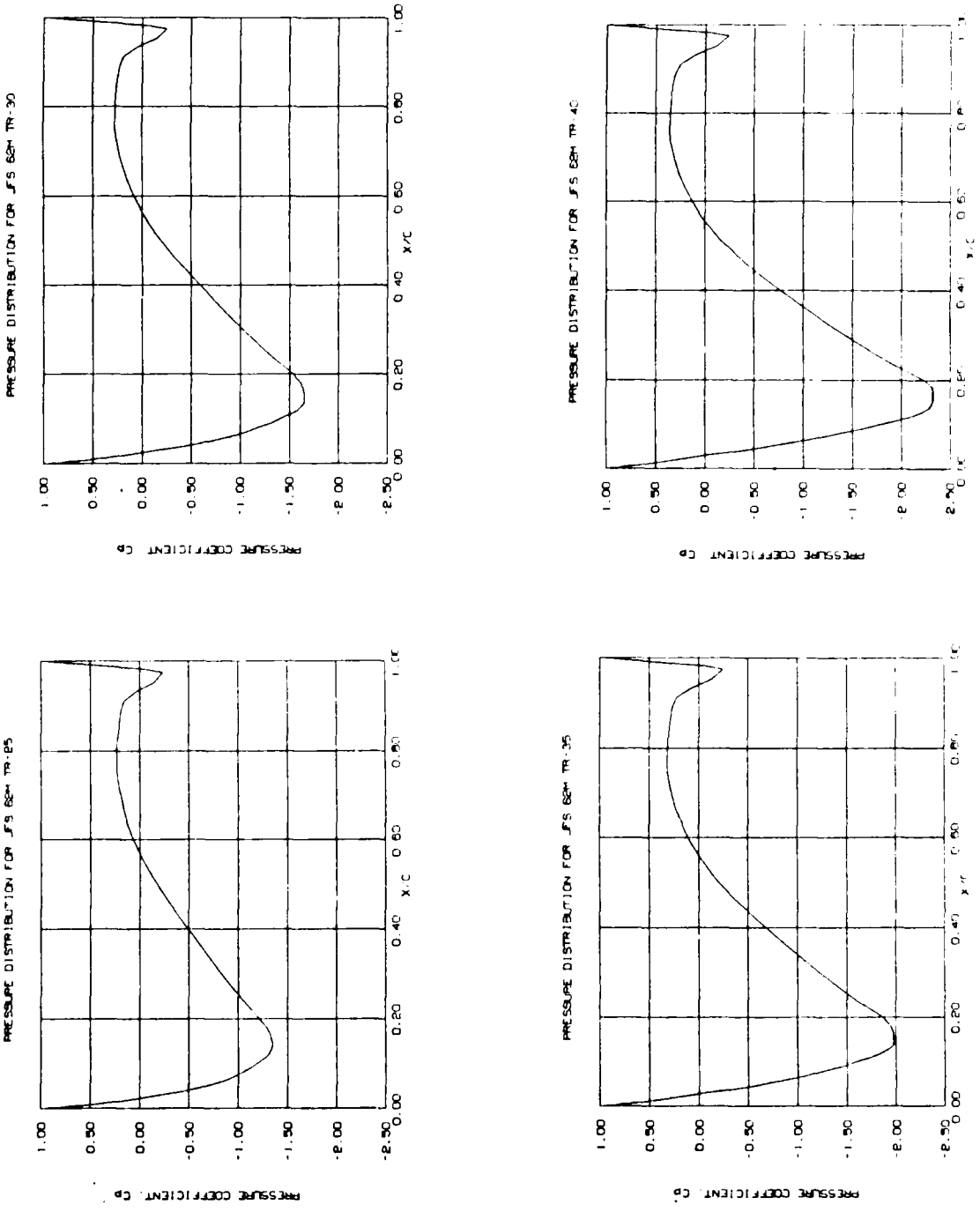

Fig. 5.2 JFS section pressure distributions

6.0 EXPERIMENTAL TECHNIQUES

6.1 Boundary Layer Visualization

Two techniques were used for flow visualization; surface tufts and the oil/ultraviolet light method. The tufts, approximately 2.5 cm in length, were used to map the areas of turbulent boundary layer separation. A matrix of the tufts was applied at 10 percent chord stations along the chord, with approximately equal spacings along the span of the model.

The second technique, based on ultraviolet light illuminated oil, was used to determine the position of transition from laminar to turbulent flow in the boundary layer, the existence of a laminar separation bubble and turbulent separation. The latter thus serves as a check on the fluorescent mini-tuft method. A mixture of kerosene (70 percent by volume), 10WO motor oil (20 percent) and vinegar (10 percent) was used along with approximately four tablespoons of fluorescent yellow pigment per pint of the liquid. The kerosene provides the base for the mixture, the motor oil slows down the rate of evaporation of the kerosene in the wind stream, and the vinegar is used to keep the powdered fluorescent pigment in suspension. It has been found that a lemon yellow pigment used in combination with a white model background results in the highest contrast. The boundary layer was viewed under 100-watt ultraviolet lights approximately 0.5 to 1.0 m from the model. Photography was accomplished with settings of f/2 to f/4 at 1/15 to 1/30 of a second.

6.2 Profile Drag - Momentum Method

The momentum loss method for determining the profile drag is well known, Pope [4]. When the momentum equation is integrated around a control volume that includes the wake, it can be shown that the drag force on the drag is given by the expression:

$$D = b\rho \int_{-\infty}^{\infty} U(U_\infty - U)dy \qquad (6.1)$$

The drag coefficient may be based on planform area (bc) as is common in aeronautical work, or on frontal area (bt), as is common practice among marine engineers. Thus:

$$C_{d_{(bc)}} = D/qbc \quad \text{(Planform reference area)} \qquad (6.2)$$

or

$$C_{d_{(tc)}} = D/qtc \quad \text{(Frontal reference area)} \qquad (6.3)$$

where

q = dynamic pressure

$= 1/2\ \rho U_\infty^2$

Using Equation 6.2, the drag coefficient equation becomes:

$$C_{d_{(bc)}} = \frac{2}{c} \int^{\infty} [(q/q_\infty)^{1/2} - (q/q_\infty)]dy. \qquad (6.4)$$

The flow conditions that the model experiences in a wind tunnel are not the same as those in free air or the open ocean. The presence of the wind tunnel walls modifies the airflow velocity over the model. The two corrections that are important in the calculation of drag coefficients are "solid blockage" and "wake blockage." Pope [4] defines the total blockage as:

$$E = Esb + Ewb \qquad (6.5)$$

where E is the sum of the solid blockage, (Esb), and the wake blockage, (Ewb).

In terms of the change in freestream velocity due to the presence of the model:

$$E = (Uo/U_\infty) - 1 \qquad (6.6)$$

where:

U_∞ = upstream velocity
Uo = downstream velocity at wake edge

Also,

$$E = \sqrt{q_o/q_\infty} - 1 \qquad (6.7)$$

where

q_∞ = upstream dynamic pressure
q_o = downstream dynamic pressure at wake edge

A correction of the wake survey drag coefficient for blockage made based on the method proposed by Shaw, Sotos, and Solano [7]. They employed the following procedure to correct for the effects of blockage:

1. The original wake survey is examined to determine the endpoints of the viscous wake.

2. The values of the velocity ratio (Uo/U_∞) for the two wake endpoints are compared, and the larger volume used to calculate a velocity ratio correction factor by subtracting 1.0 from this value.

3. All velocity ratio values contained within the viscous wake are adjusted by subtracting the velocity ratio correction factor prior to computing the section drag coefficient.

The wake data were corrected for blockage in the following manner:

Experimentally determined values of the blockage, E, were used for the drag coefficient, which was then computed using the NASA method

$$C_{d_{(bc)}} = 2 \int_{-Y}^{Y_o} \left[\left(\frac{U}{U_\infty} - E\right)\left(1 - \frac{U}{U_\infty} + E\right)\right] dy \qquad (6.9)$$

where:

U = wake velocity
dy = distance across wake.

The integration required by Equation 6.9 was accomplished using the Fritsch-Carlson [8] formulas for piecewise cubic data interpolation and Gauss-Legendre Quadrature numerical integration.

6.3 Profile Drag-Balance Method

A series of equations were used to correct for balance interaction between the measured lift, drag, and pitching moment. These equations were:

$$\begin{aligned} L &= 1.0040\ (Lr) + 0.0004\ (Mr) \\ D &= 0.9881\ (Dr) + 0.0020\ (|Lr| - 0.0002\ Mr) \\ M &= 1.0000\ (Mr) + 0.0753\ (Lr) \end{aligned} \qquad (6.10)$$

where L_r, D_r, and M_r are the lift, drag, and pitching moments values uncorrected for blockage.

6.4 Hydrodynamic Center

A visual measurement was made of the equilibrium angle of attack (yaw angle) of the fairing section as a function of the chordwise mechanical pivot location to determine the hydrodynamic center location. When the pivot point is forward of the hydrodynamic center, the fairing will remain aligned with the flow, exhibiting "weathervane" stability and the angle of attack will be zero degrees. The pivot location was moved progressively aft in steps of 0.05 c. At each pivot position, the equilibrium angle of attack was recorded. The angles were measured using the protractor that was inscribed in the plexiglass top of the wind tunnel. The accuracy of the readings was $\pm 0.5°$.

When the pivot position is moved aft of the hydrodynamic center, the fairing will assume an equilibrium angle of attack other than zero degrees. This equilibrium angle will be positive or negative, depending on the direction of the initial disturbance. Because the step size between pivot positions was 0.05 c, the hydrodynamic center was located by this technique with an accuracy of +0.025 c.

7.0 EXPERIMENTAL RESULTS

7.1 Boundary Layer Visualization

The tuft patterns were photographed at a shutter speed of 1/30 of a second. The existence of turbulent boundary layer separation would be indicated by a blurring of the tuft pattern.

The oil coat was applied liberally with the air stream turned off. After bringing up power, the tunnel would reach a steady state velocity at the low Reynolds No. (q = 0.5 psf) in 30 to 60 seconds. For the higher Reynolds No. (q = 9.0 psf), an equilibrium speed would not be reached for four to five minutes because of the time required to sequence the power build up. Consequently, the oil excess would run down the aft portion of the model, as seen in the photographs.

7.1.1 JFS 62M TR-25:

The TR-25 section was tested at Reynolds numbers of 1.27, 1.81, 2.84, 3.35, 4.0, 4.69, 5.3 x 10^5. The results of the tuft studies viewed from above the model and the oil ultraviolet light studies viewed from the side, are shown in Figs. 7.1 and 7.2. The tuft studies show no boundary layer separation. It was observed during testing that there was a slight lateral movement in the spanwise direction; however, there was no surface lifting of the tufts, even in the pressure recovery area of the foil section.

The oil ultraviolet studies were useful in showing the existence of the laminar separation bubble and the extent of the laminar and turbulent boundary layers. The boundary layer was assumed to be fully attached from the leading edge up to the point where the dark stripe is shown from approximately 20 to 30 percent of the chord. The dark striped area indicates the existence of the laminar separation bubble, and is indicative of the fact that the oil excess is not being swept away. Aft of the laminar separation bubble, turbulent reattachment of the boundary layer occurs to the trailing edge.

The TR-25 section displayed the longest separation bubble at low Reynolds numbers covering approximately 14% of the chord length, Fig. 7.3. The transition point moved forward to about X_t/c = .25 at high Reynolds numbers. No separation was observed. As the Reynolds number increases, the area of the laminar separation bubble is seen to decrease in size, until at a Reynolds number of approximately 3.35 x 10^5, it has disappeared completely, indicating that transition occurs over a very short length.

7.1.2 JFS 62M TR-30:

The results for the TR-30 section are shown in Fig. 7.3. The transition point moved towards the leading edge to about X_t/c = 0.25. The laminar separation bubble at Re = 1.26x10^5 covered more than 12 percent of the chord length. No turbulent boundary layer separation was observed from the surface tuft studies. It should be noted that the laminar separation bubble begins approximately at the point of maximum thickness (20 percent chord).

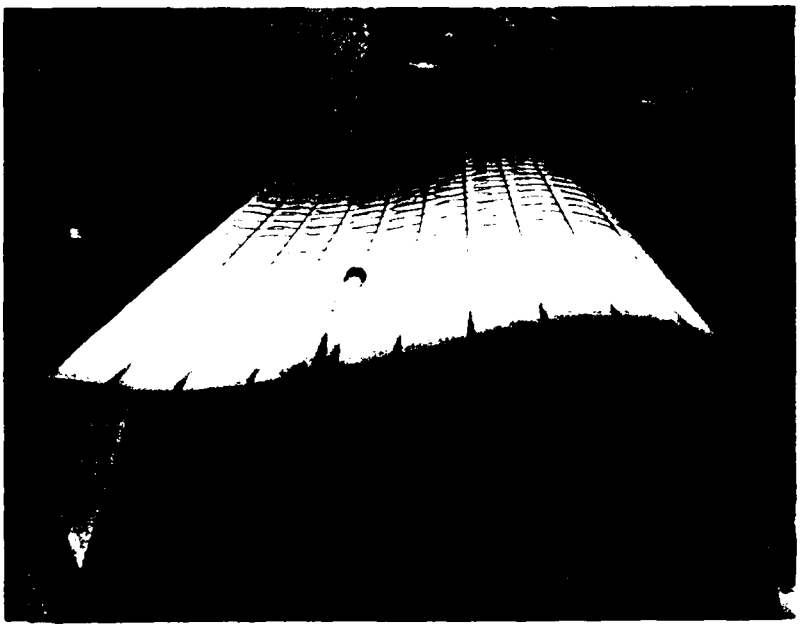

Q = 0.5 psf

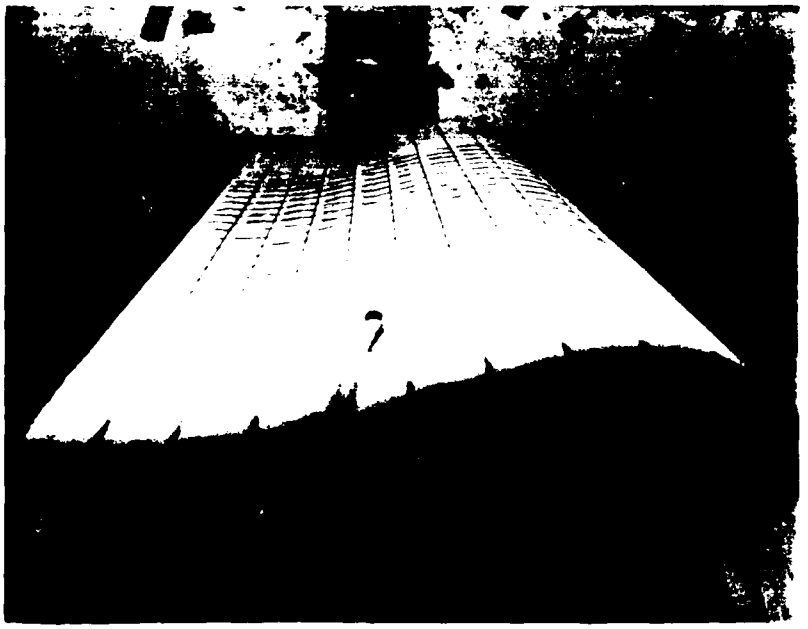

Q = 9.0 psf

Fig. 7.1 JfS 62M TR-25 - tuft boundary layer results

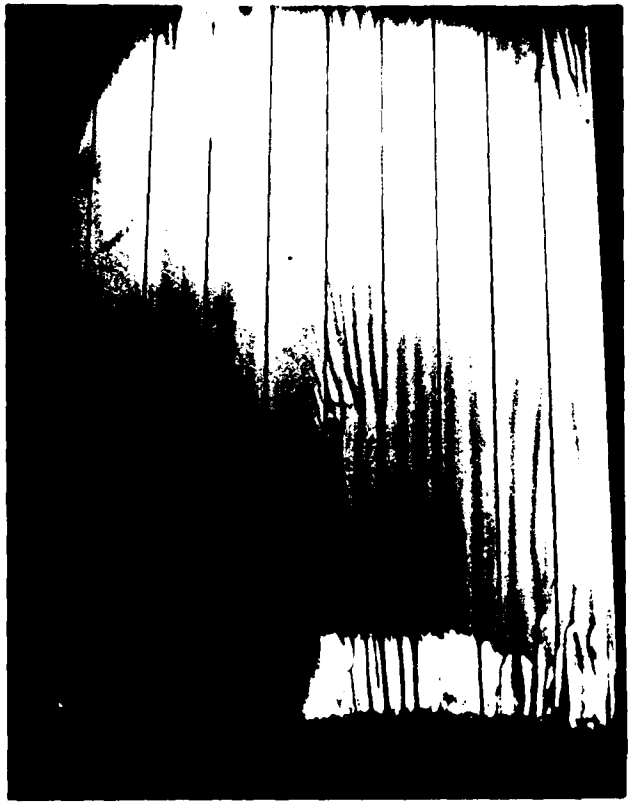

Q = 0.5 psf

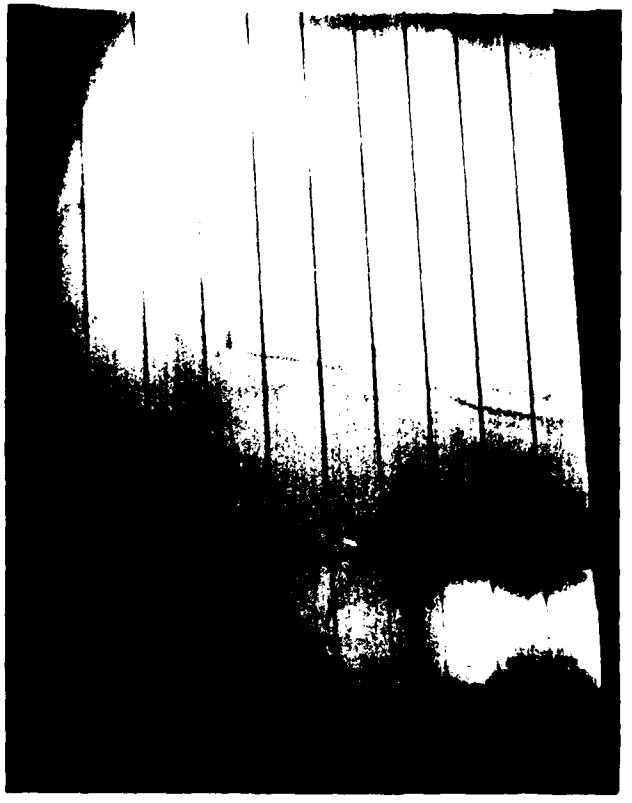

Q = 9.0 psf

Fig. 7.2 JfS 62M TR-25 - oil/uv light boundary layer results

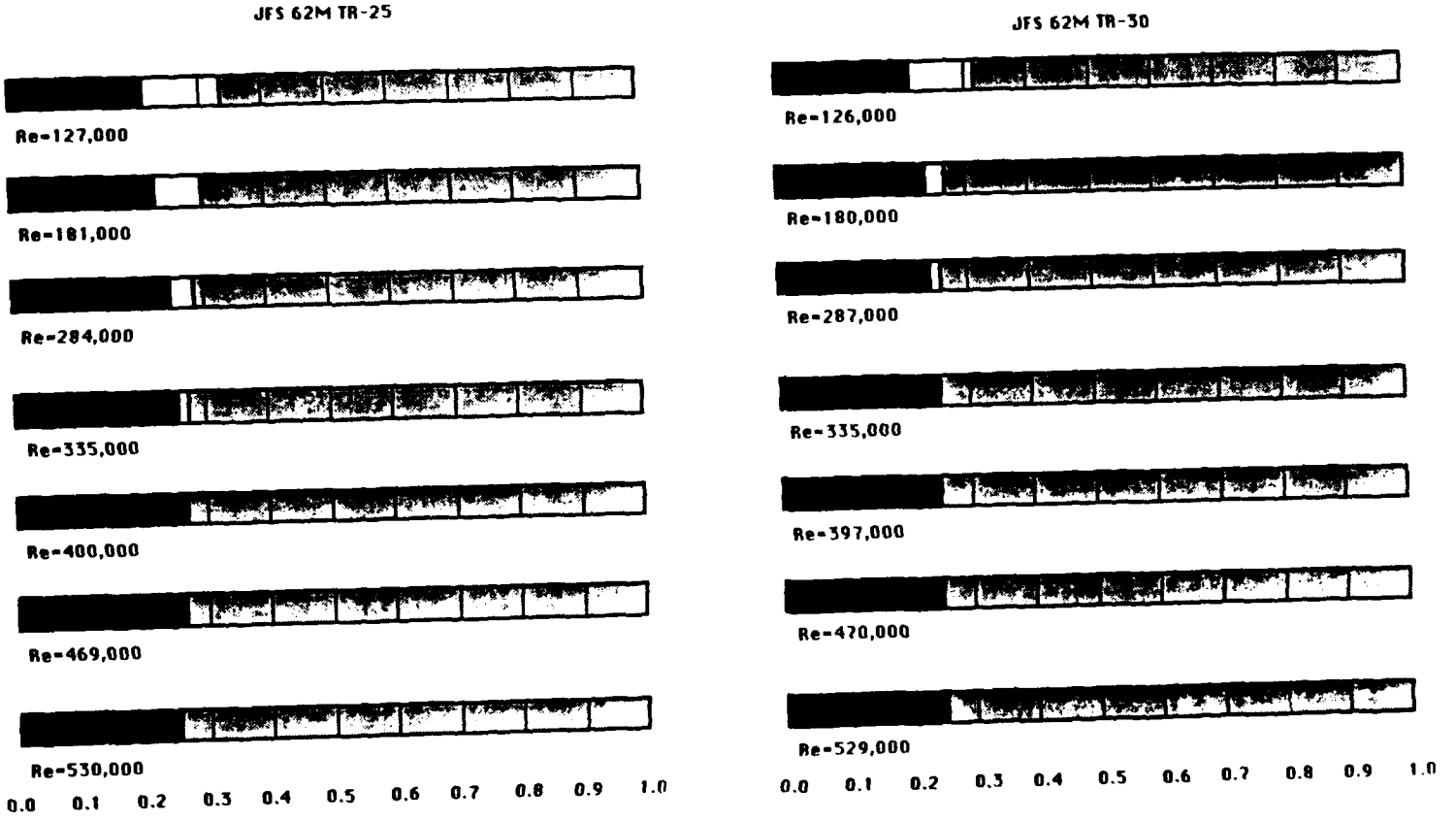

Fig. 7.3 Boundary layer summary

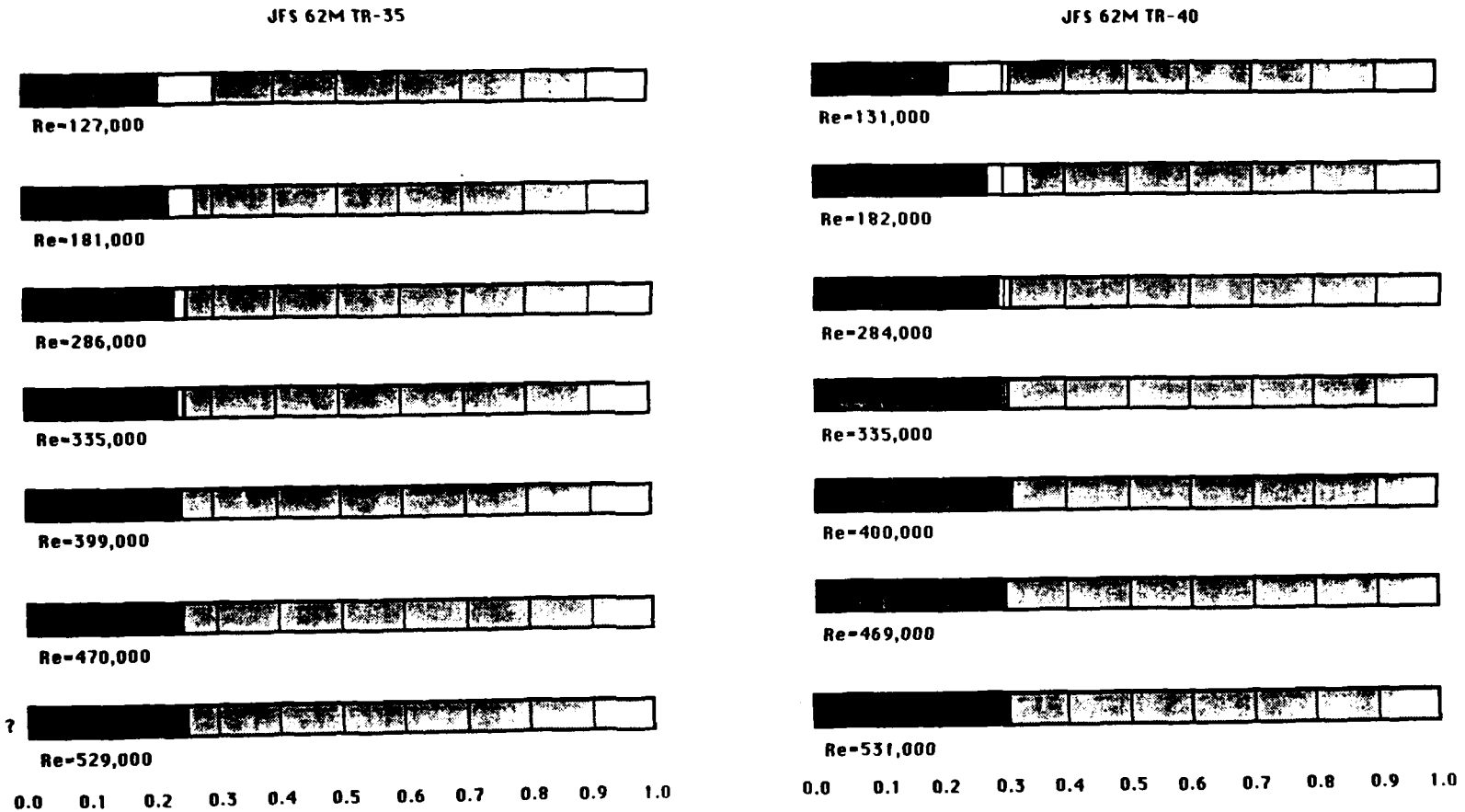

Fig. 7.3 continued

This corresponds to a position slightly downstream of the peak pressure point which occurs at about 15 percent of the chord.

7.1.3 JFS 62M TR-35:

A short laminar separation bubble was visible at Reynolds numbers from $1.27x10^5$ to $3.99x10^5$, Fig. 7.3. At the lower Reynolds number, the laminar separation bubble extended from x/c = .22 to .31, tapering to a thin line at $Re = 3.99x10^5$. The transition point moved towards the leading edge with increasing Re to about $X_t/c = .25$. No separation was observed. In all cases, transition occurred aft of the point of minimum pressure point at x/c = .18 and aft of the maximum thickness at x/c = .2. The transition point moved towards the leading edge as the Reynold's number increased.

7.1.4 JFS 62M TR-40:

The results of the boundary layer visualization for the TR-40 section agree with the previous work of Calkins and Gray, Figs. 7.4 and 7.5. The fluorescent dye technique revealed the presence of a short laminar separation bubble at low Reynolds numbers $1.31x10^5$ to $3.35x10^5$. Transition occurred at $X_t/c = 3.0$ at $Re = 1.31x10^5$, then moved aft at $1.82x10^5$ before moving towards the leading edge for the remainder of the flow speeds.

7.2 Profile Drag Coefficient-Balance Method

A comparison between the measured balance drag data and previously published wake drag coefficients for the JFS 62M section revealed a discrepancy. The balance data showed higher drag values due to endwall junction losses. Flow visualization using tufts confirmed the presence of 3-Dimensional horseshoe vortices.

7.2.1 Horseshoe Vortices

Many authors have investigated the losses due to the intersection between a three-dimensional strut and a planar surface. These losses are generated by a three-dimensional flow phenomenon known as a horseshoe vortex. Horseshoe vortices have been observed at a wing-fuselage junction, at the leading edge of a turbine blade near an endwall and around the bases of bridge piers set in a river bed. Typical investigations have included both flow visualization and quantitative measurements of the velocity field, but very few authors have generated predictive models of these losses. In particular, there are no methods to determine the effect of the horseshoe vortices on the lift, drag, and pitching moment characteristics of a 2-D symmetrical bluff body. This study found that the horseshoe vortex precluded the generation of "pseudo" infinite aspect ratio flow over the endplated model.

The horseshoe vortex is a complex 3-D flow resulting from the intersection of a strut with the boundary layer along a planar surface. Three mechanisms are thought to generate these secondary flows:

1. Reynolds-stress components in turbulent or viscous flow (Shabaka and Bradshaw, [9])

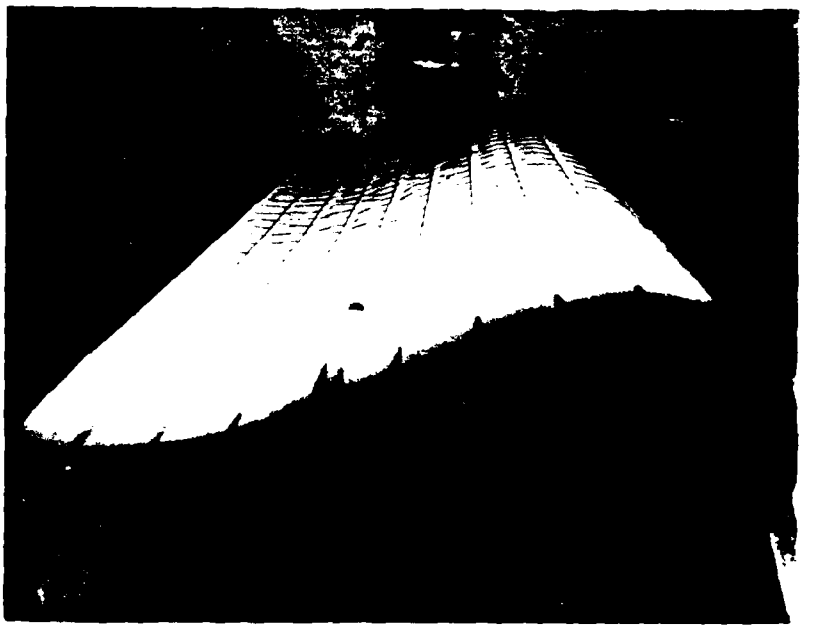

Q = 1.0 psf

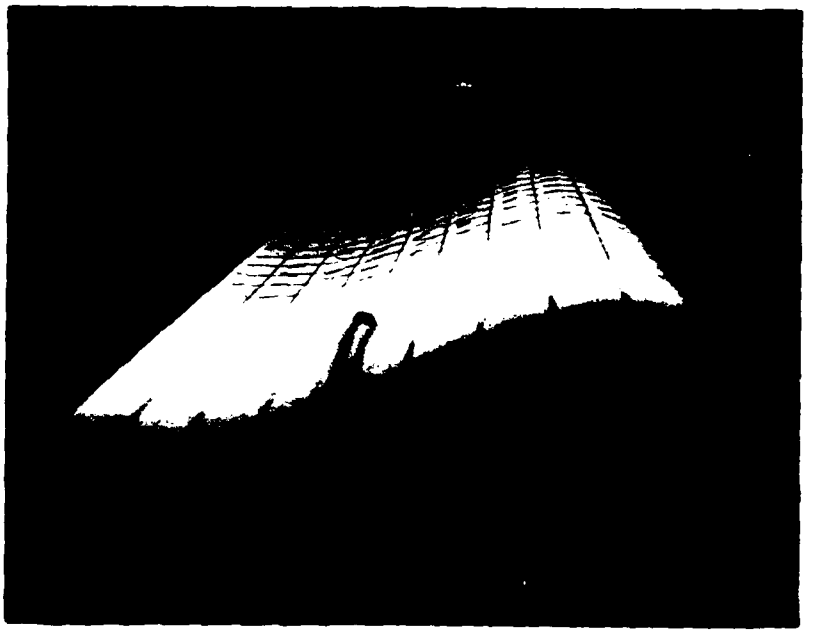

Q = 9.0 psf

Fig. 7.4 JfS 62M TR-40 - tuft boundary layer results

Q = 1.0 psf

Q = 9.0 psf

Fig. 7.5 JfS 62M TR-40 oil/uv light boundary layer results

2. lateral deflection or skewing of the streamlines in the shear layer (Mehta, Shabaka and Bradshaw, [10])

3. separation of the approaching boundary layer upstream of the intersecting strut (Kuchemann, [11]).

Shabaka and Bradshaw, [9] report that "Reynolds-stress induced secondary flows are slow to develop, while skew-induced secondary flows are slow to be attenuated by Reynolds stresses." The skew-induced vortex dominates the corner flow to the trailing edge. Baker [12] and Belik [13] have shown that boundary layer separation upstream of the intersecting strut is a possibility. The approaching boundary layer along the planar surface is unable to run up against the adverse pressure gradient generated by a blunt body. The boundary layer separates at the singular separation point upstream of the junction, and is wrapped into a vortex sheet which is subsequently swept around the body in the characteristic horseshoe shape with streamwise vorticity. A secondary stagnation point is located on the leading edge of the strut at some spanwise distance from the endwall. Han, Ma and Rapp, [14] and Johnson [15] have excellent illustrations of the horseshoe vortex separation loci. The extent to which this complex flow in the strut/wall junction disrupts the 2-D flow over the bluff body determines the affect on the lift, drag, and pitching moment characteristics of the shape in question.

Barber [16] has identified two mechanisms controlling strut surface flow and intersection losses that depend on the upstream boundary layer thickness and the size of the resultant horseshoe vortex, Fig. 7.6. A thin boundary layer results in:

1) large intersection loss
2) strong dependence on flow incidence angle
3) very small horseshoe vortex

A thick boundary layer, in contrast, results in:

1) small intersection loss
2) weak loss dependance on flow incidence angle
3) large horseshoe vortex

Unfortunately, these observations are not quantified in terms of foil geometry or aerodynamic characteristics.

7.2.2 Flow Field/Balance Measurements

Photographs of the horizontally oriented two-dimensional JFS 62M TR-40 model with tufts for flow visualization, Fig. 7.7, clearly indicate three-dimensional surface flow at the strut/endwall junction. The tuft patterns supports the results of the flow visualization studies of Han and More [16] and confirm the presence of horseshoe vortices at both junctions. The upper limit of the horseshoe vortex is growing in a spanwise direction downstream of the leading edge and the tufts indicate surface shear velocities in the direction of the endwall, Fig. 7.7. The overall pattern is very similar to Johnson's [14] diagram of horseshoe vortex growth for thin boundary layer.

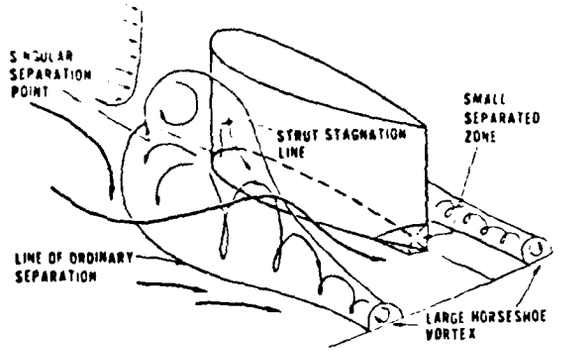

thick boundary-layer-strut interaction.

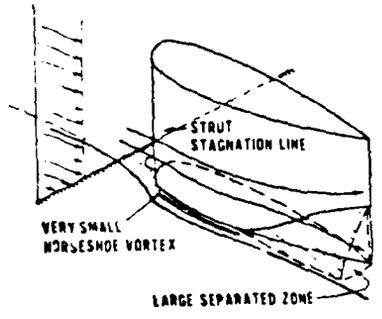

thin boundary-layer-strut interaction.

Fig. 7.6 Model/wall horseshoe vortex

Balance measurements made on the JFS 62M TR-40 section confirm Barber's [16] observations on the role played by the boundary layer on intersection losses. An investigation was performed of the effect of the model/endwall gap on the drag of the TR-40 section. Three tests were performed:

1) TR-40 with no endwalls,
2) TR-40 with a 3/4" gap between the model and the endwalls, and
3) the TR-40 with <1/16" gap.

The gap size was controlled using shims of known thickness during the placement of the 2-D walls. The results, presented in Fig. 7.8, demonstrate that the drag increases with decreasing gap thickness. The junction losses are increased as the strut penetrates the flat plate boundary layer. Calculations based on flat plate theory using the momentum equation suggest a boundary layer thickness of 5.00 cm (2 in.) for mid-range Reynold's numbers. The 1.91 cm (3/4") gap data has the same slope as the no gap data suggesting the influence of the 2-d wall on the edge vortices act to increase the drag. The <0.16 cm (1/16 in.) data indicates that the model has penetrated the boundary layer and that junction losses are now dominating the drag.

7.3 Profile Drag Coefficient - Momentum Method

Velocity surveys, both upstream and downstream of the model, were made in order to compute the profile drag coefficient using the momentum wake deficit technique. The effect of the model on the transverse velocity profile is shown in Figure 7.9.

7.3.1 Upstream Velocity Profile

Ideally, upstream of the model, the velocity profile must be uniform across the model, Fig. 7.9. Figures 7.10 shows the measured uniform velocity upstream of the model as function of the corrected indicated dynamic pressure measured by the tunnel. The figures show the effect of model thickness to chord ratio on the value of the upstream velocity. It may be seen that there is a linear relationship such that the tunnel indicated dynamic pressure is exactly equal to the wake measured dynamic pressure for the 25 percent thickness to chord ratio model. As the thickness to chord ratio increases, it is seen that at approximately an indicated dynamic pressure of 3 psf, the upstream pressure is slightly less than the indicated pressure. This is due to the effect of the model on the upstream dynamic pressure distribution. The actual upstream pressures measured by the wake were used in all subsequent calculations for the blockage.

7.3.2 Downstream Wake Profile

Wake profiles were made downstream of the model at a position determined to be such that the static pressure measured in the transverse wake profile was equal to that upstream of the model. Figures 7.11 and 7.12 show the wake profiles for the 25 percent and 40 percent thickness to chord ratio models over at the extremes of the Reynolds number range that were tested from approximately 125,000 to 530,000, with a mid-range velocity profile shown for comparison. These data were used to compute the blockage in percentage as a function of Reynolds number.

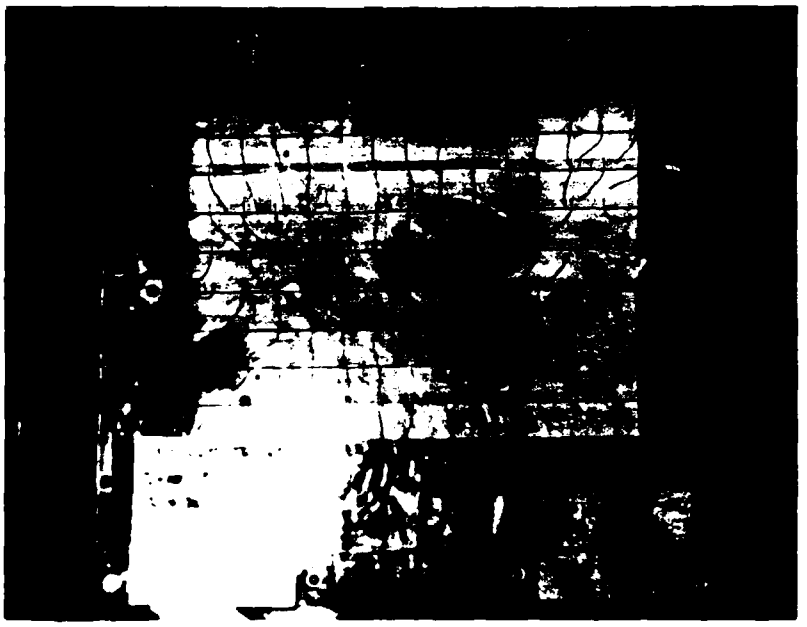

Q = 1.5 psf

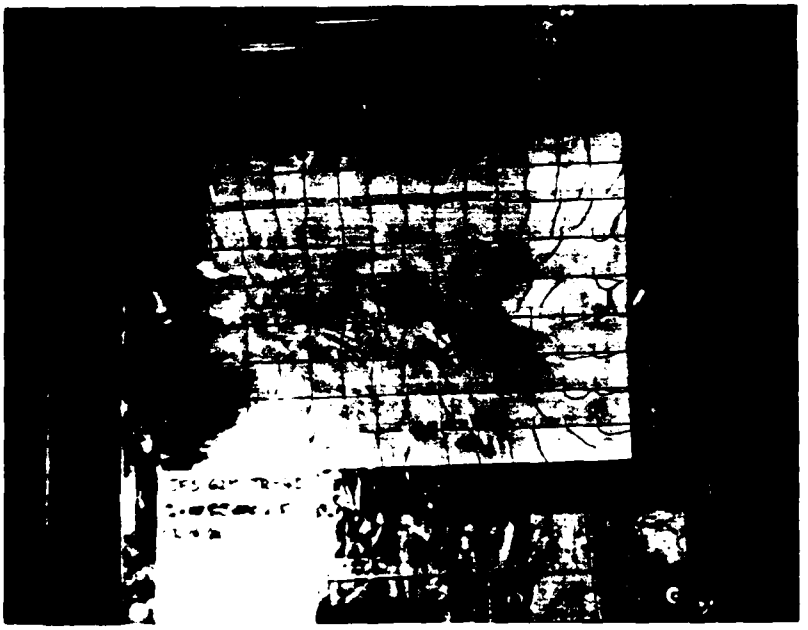

Q = 2.5 psf

Fig. 7.7 Fairing section horseshoe vortex

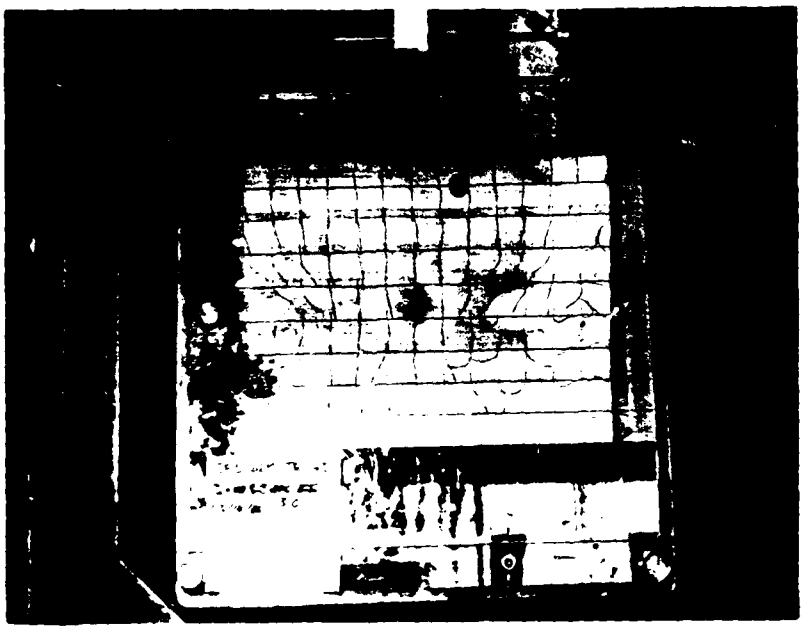

Q = 3.0 psf

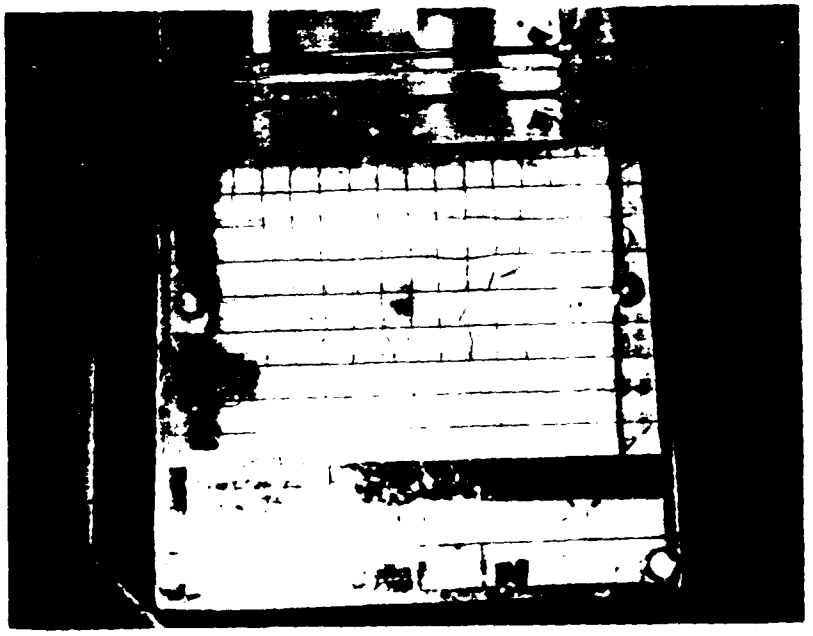

Q = 4.0 psf

Fig. 7.7 continued

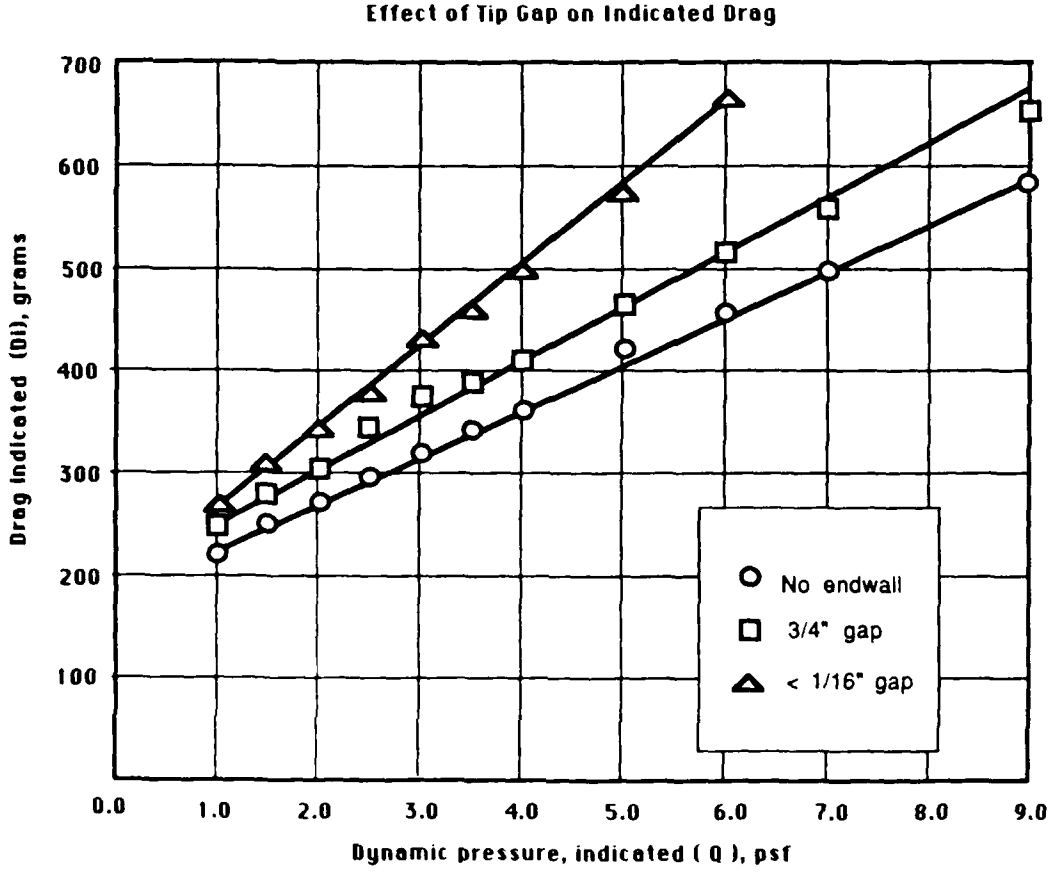

Fig. 7.8 Effect of tip gap on indicated drag

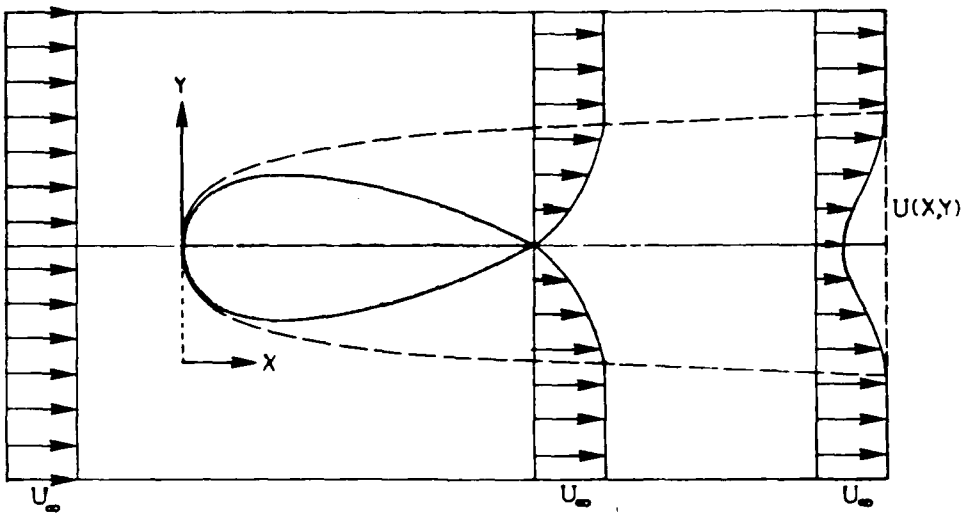

Fig. 7.9 Model wake profiles

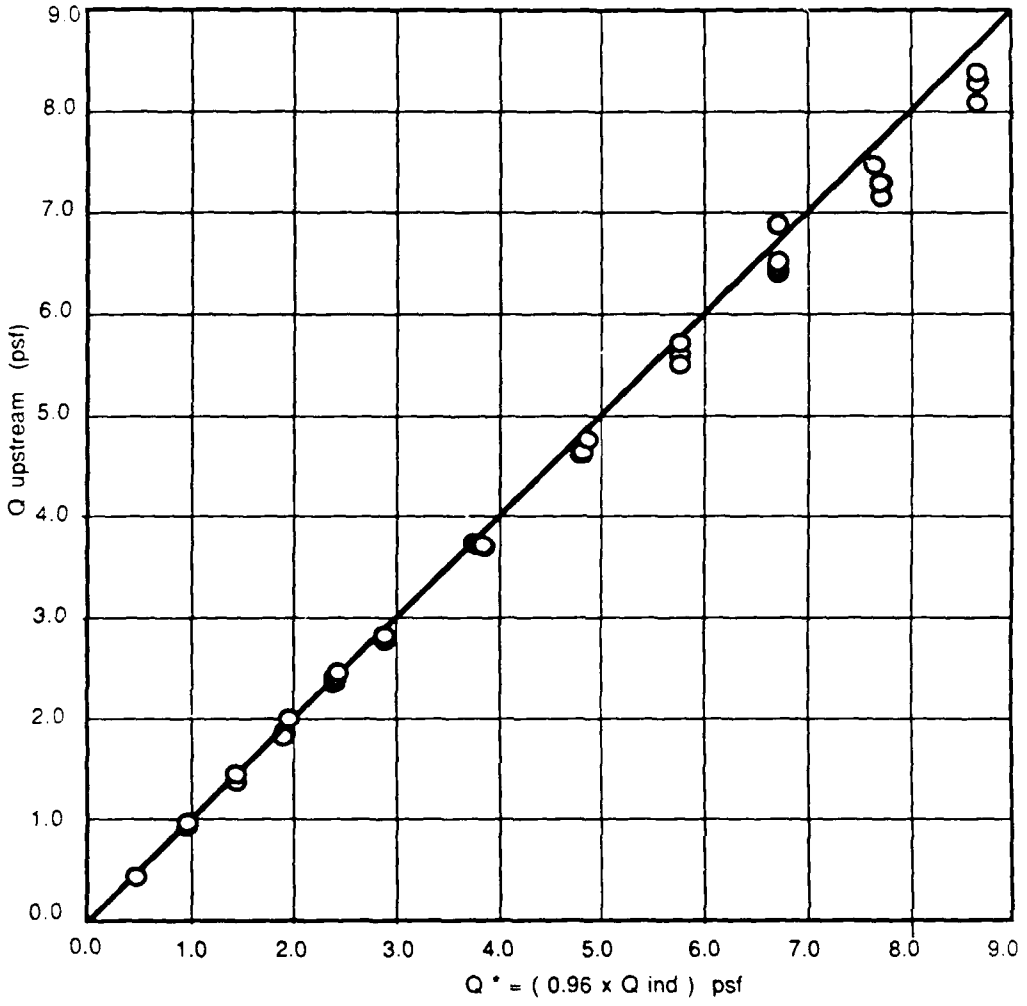

Fig. 7.10 Upstream dynamic pressure as a function of tunnel indicated dynamic pressure

It is interesting to compare the blockage results for the 40 percent thickness to chord ratio model with the previous results obtained in phase (1), Fig. 7.13. It is seen that the percent blockage is lower by a significant amount, approximately one third the values previously reported. However, when compared with the theoretically predicted blockage, Fig. 7.14, it is seen that the measured values are in good agreement. The theoretically prepared blockages were computed according to the theory by Pope [4]. Finally, Figure 7.15 shows the blockages for the remaining three models. Unfortunately, the data do not show the same trend as that of the 40 percent thickness to chord ratio.

7.3.3 Profile Drag Coefficient

The profile drag coefficients at zero degrees angle of attack are presented as a function of Reynolds number in Figures 7.16 through 7.22. They are presented based on two reference areas: the planform area, bc, and the frontal area, bt. Figure 7.20 shows the composite planform area based profile drag coefficients for the four models including the data for the 40 percent thickness to chord ratio model, from the Phase (1) studies. It is immediately noted the discrepancy between the Phase (1) results and the Phase (2) results. Phase (2) results like the previously discussed blockage results are lower.

Figure 7.17 compares the profile drag coefficients based on frontal area for both the Phase (1) and Phase (2) results. Again, especially at the lower Reynolds number, the phase (1) results are seen to be significantly higher. Basing the drag coefficient on frontal area leads to a confusing plot for the remaining t/c sections. Consequently, additional information is presented in Figure 7.18 which shows the profile drag coefficient based on frontal area as a function of thickness to chord ratio for Reynolds number values of 1.27, 1.8, 2.19, 2.54, 2.86, 3.13, 3.57, 3.99, 4.35, 4.7, 5 and 5.29 x 10^5. It is seen that as the Reynolds number increases, the tendency is to show that the minimum profile drag coefficient occurs at thickness to chord ratios between 30 and 35 percent.

7.4 Hydrodynamic Center Location

7.4.1 Yaw Stability States

An important factor for high speed towing systems is the weathervaning behavior of the fairing to prevent tow-off or kiting. Henderson [17] reports that fairing angles of attack (Yaw) as small as 0.1° can result in significant tow-off angles. Fairing sections must satisfy the following criteria:

1. the location of the mechanical center of rotation must be considered with respect to the fairing's chordwise position of maximum thickness,

2. the hydrodynamic center must be aft of the mechanical center of rotation to ensure weathervaning capability,

3. hydrodynamic restoring moments must be high to overcome friction between the fairing and the mechanical pivot,

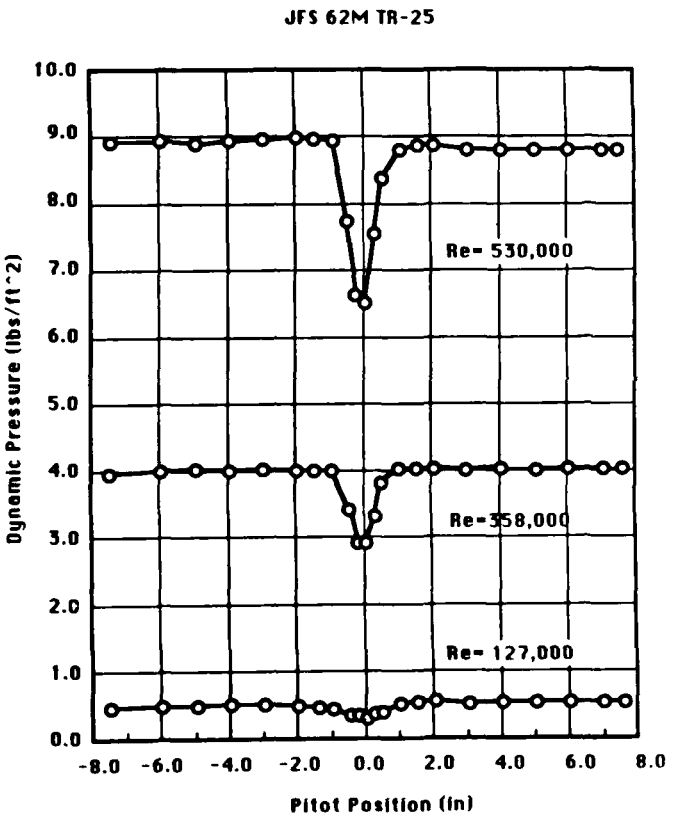

Fig. 7.11 JfS 62M TR-25 wake profiles

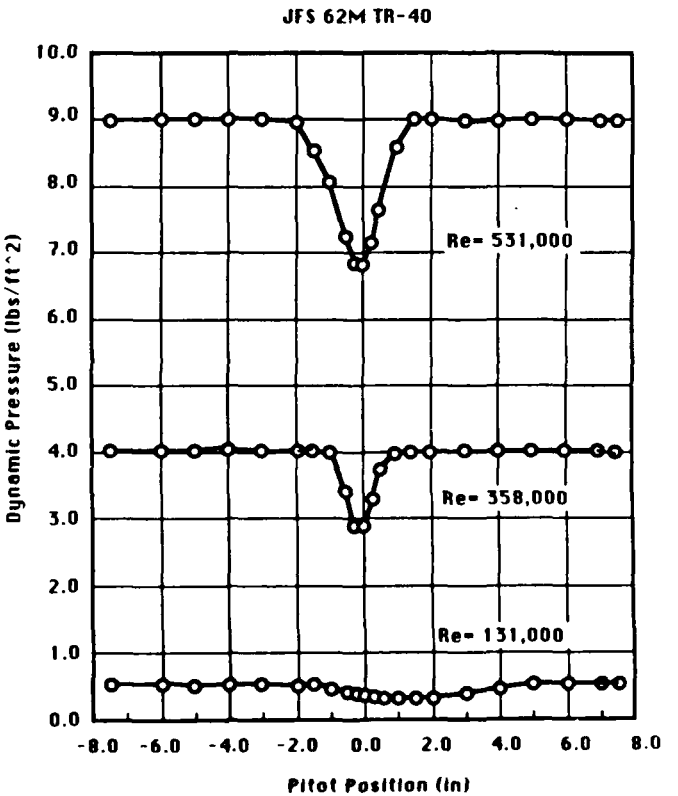

Fig. 7.12 JfS 62M TR-40 wake profiles

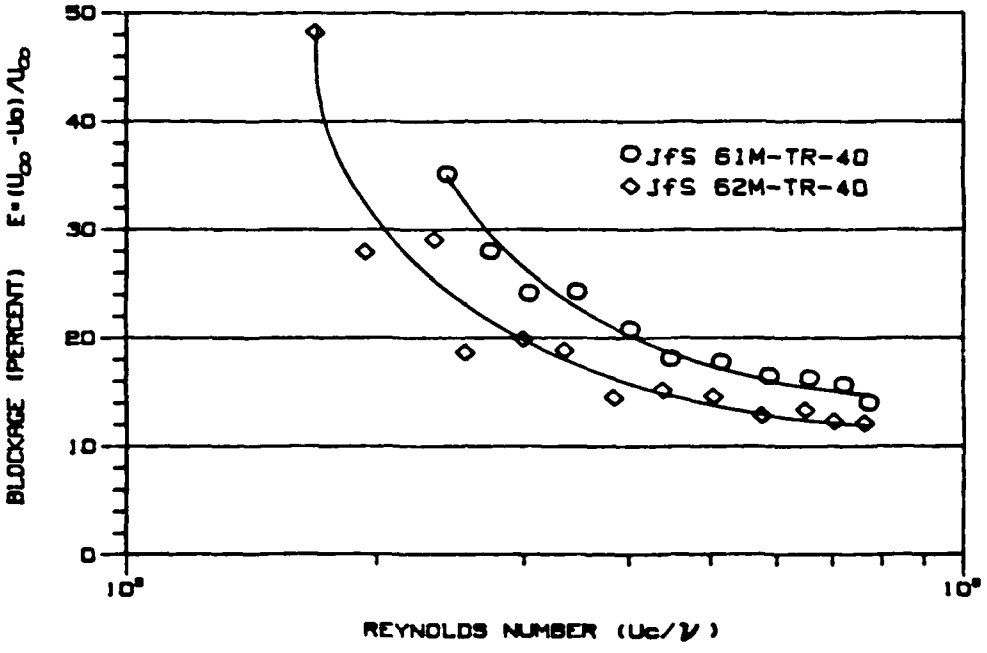

Fig. 7.13 Measured blockages of the JfS 40 section

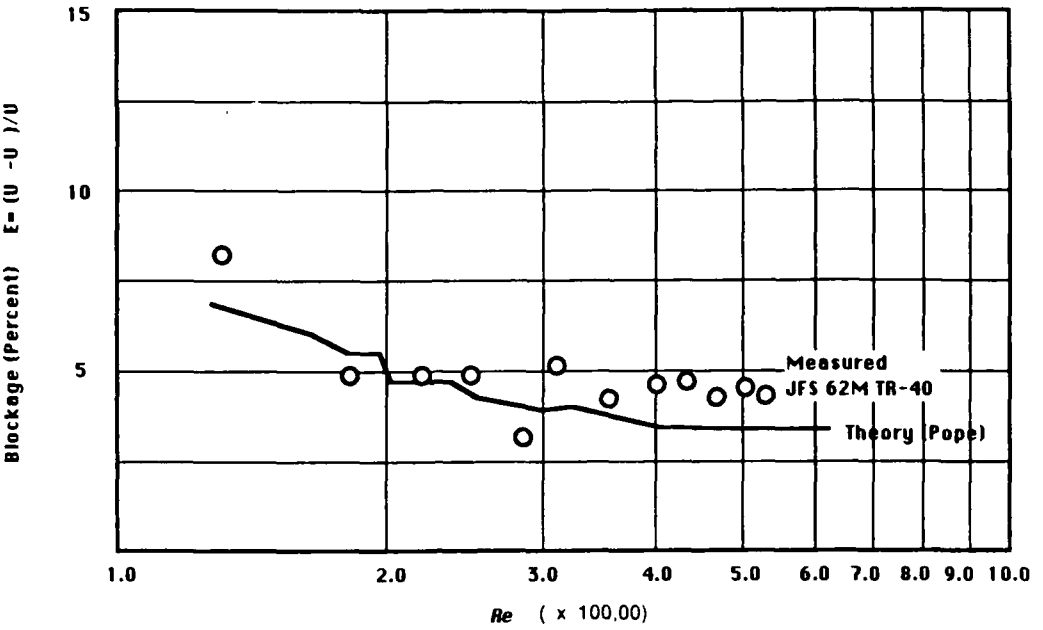

Fig. 7.14 Blockage comparison with theory

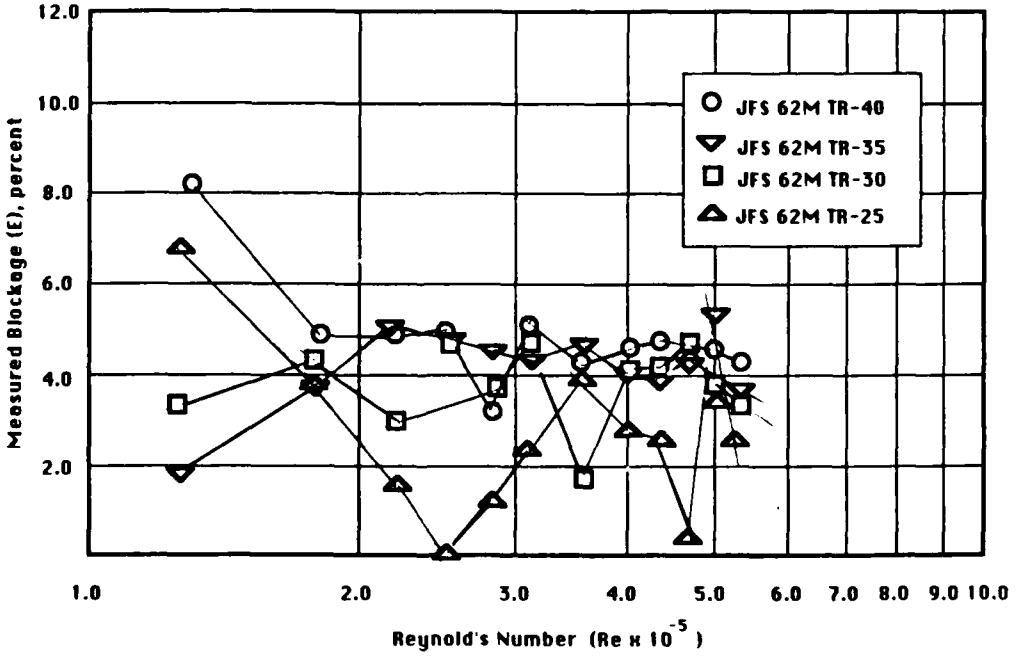

Fig. 7.15 Blockages for t/c family

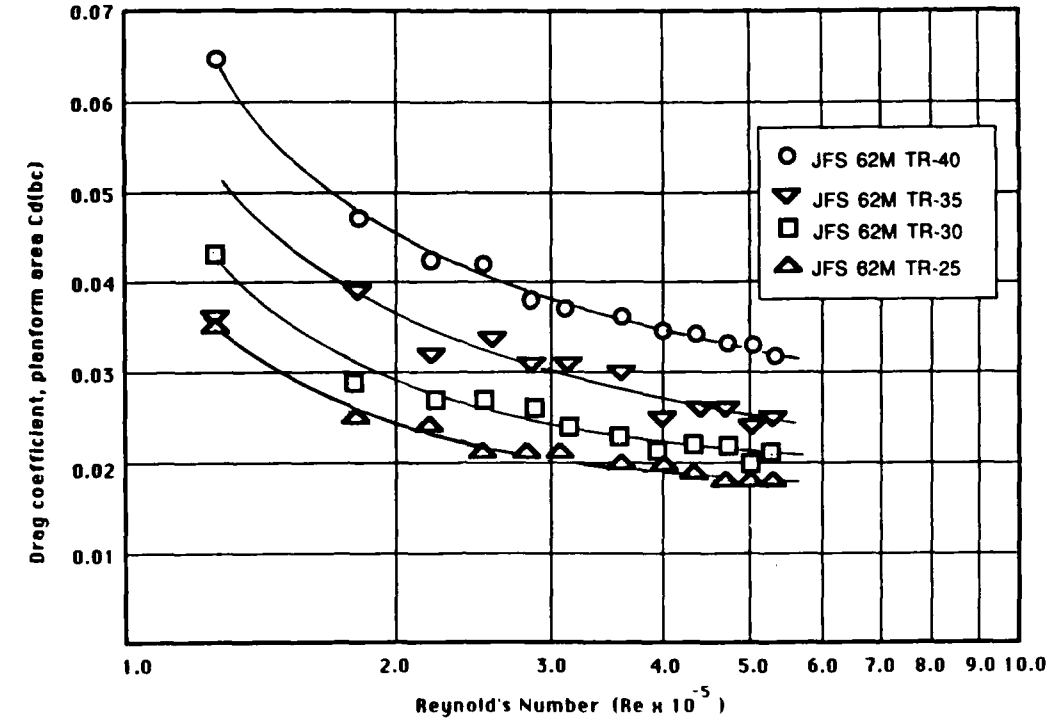

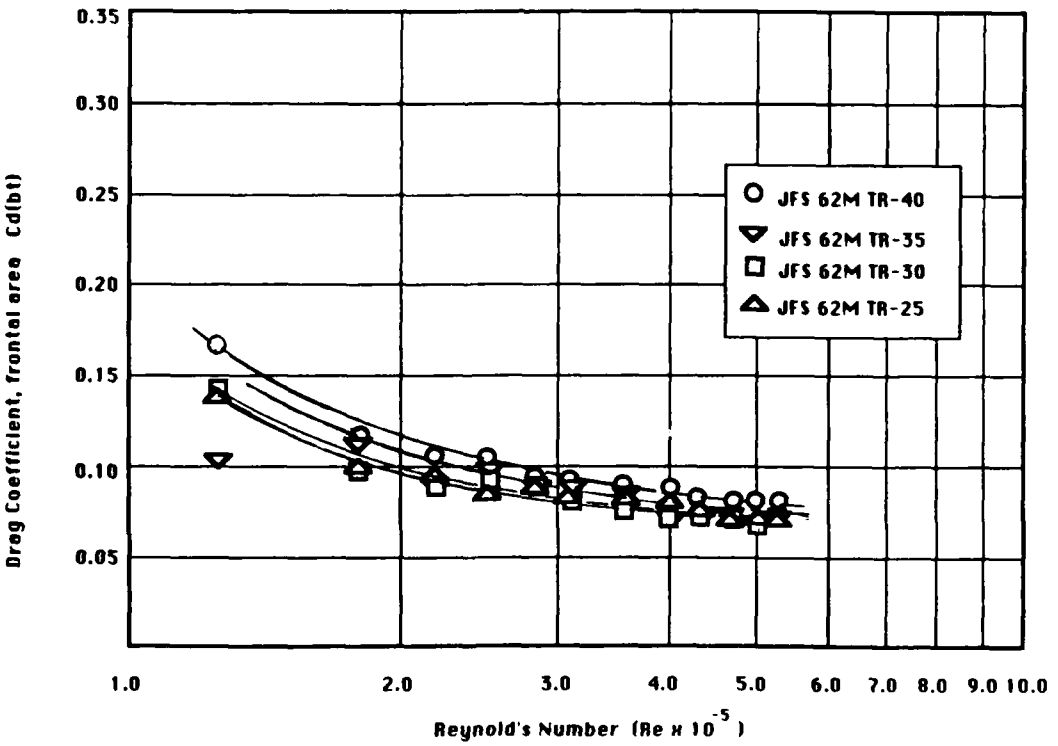

Fig. 7.16 Plan form area profile drag coefficient

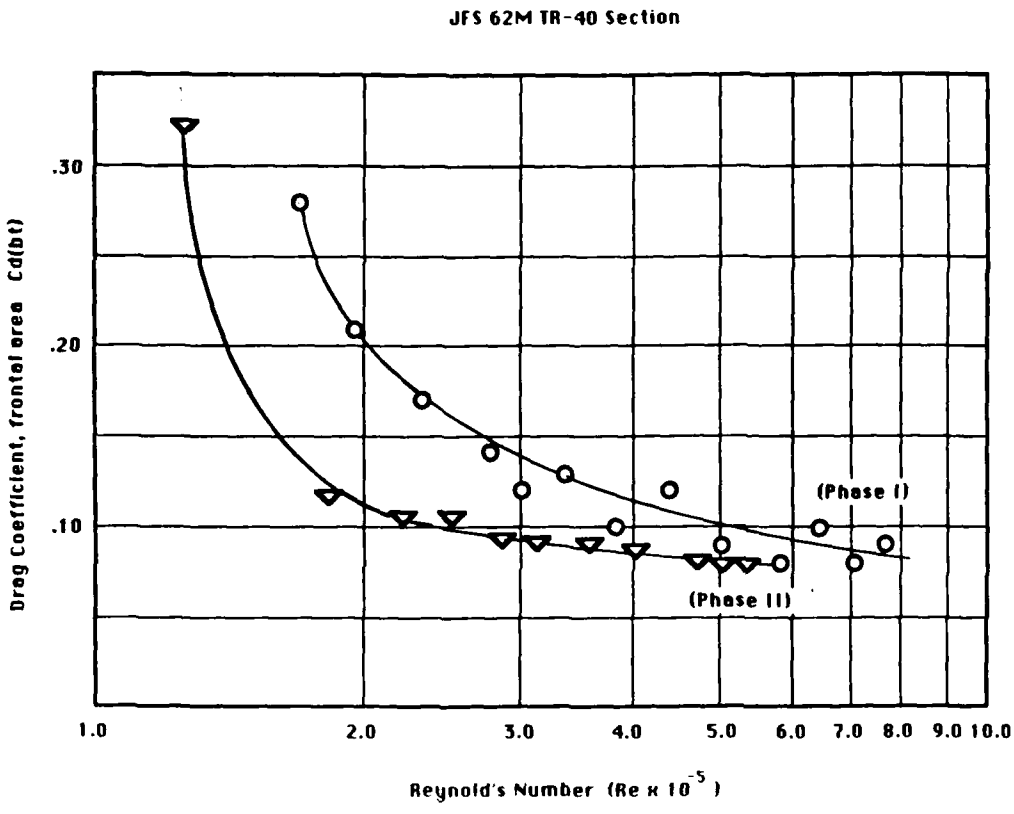

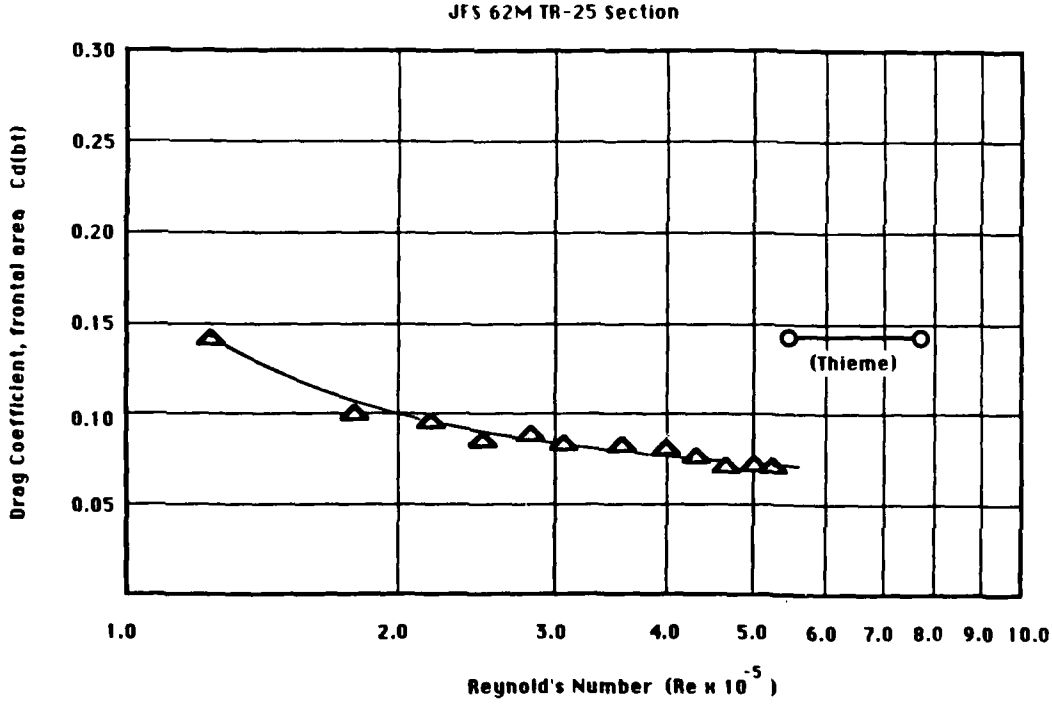

Fig. 7.17 Frontal area profile drag coefficient comparison

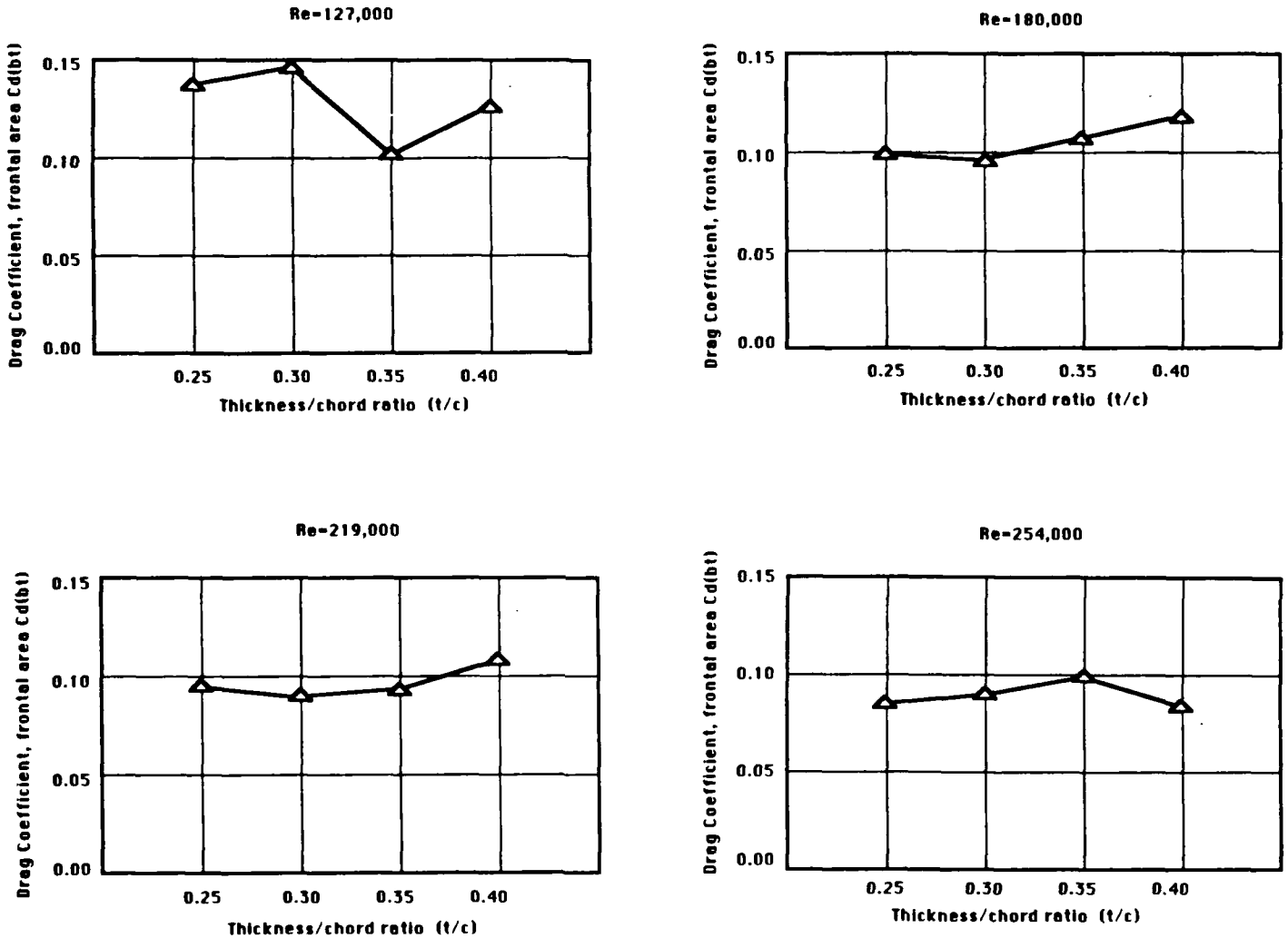

Fig. 7.18 Profile drag coefficients as a function of thickness/chord ratio

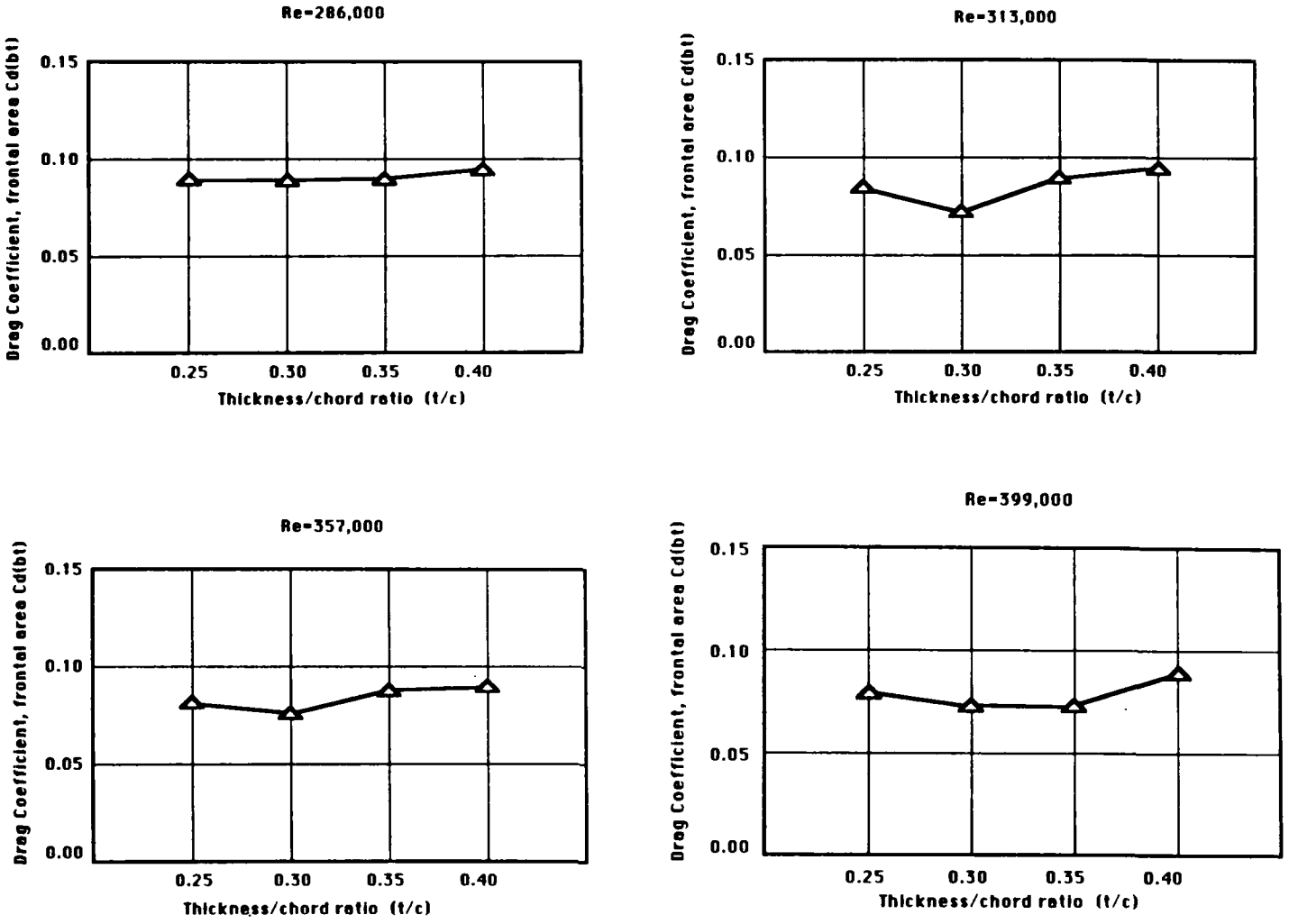

Fig. 7.18 continued

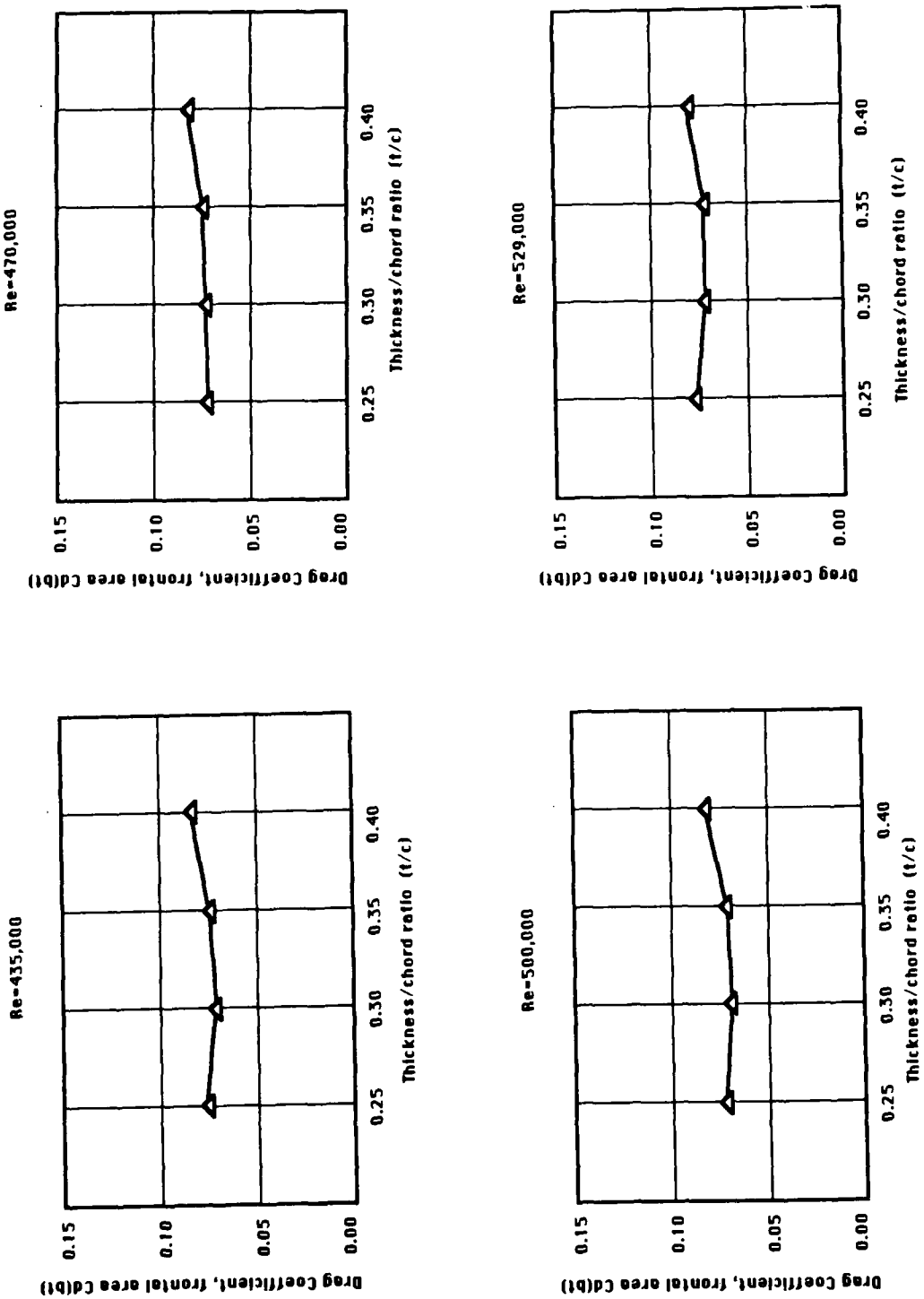

Fig. 7.18 continued

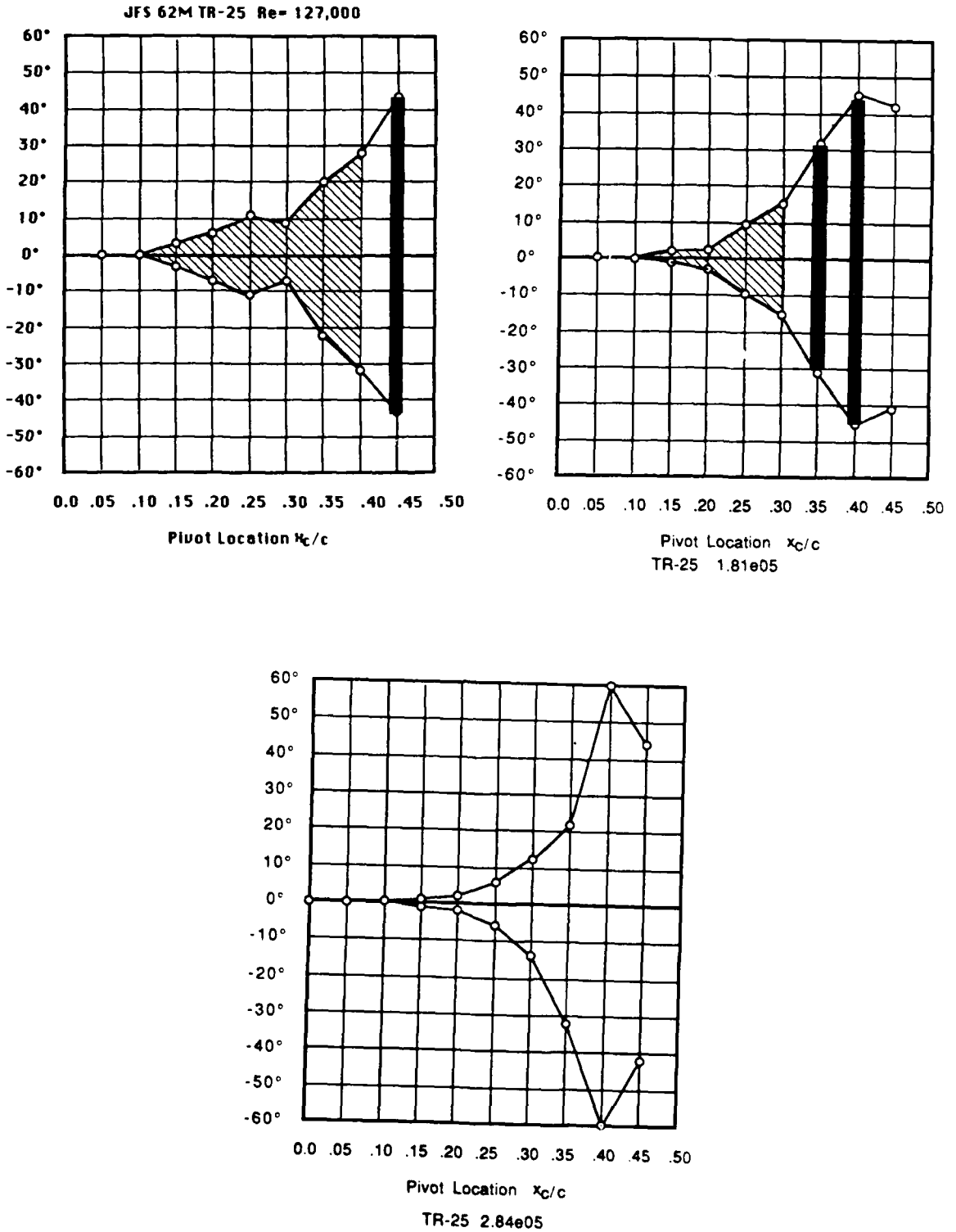

Fig. 7.19 JfS 62M TR-25 yaw stability

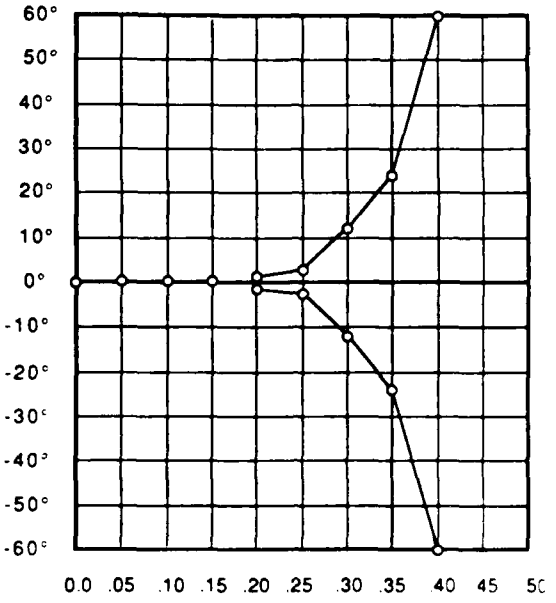

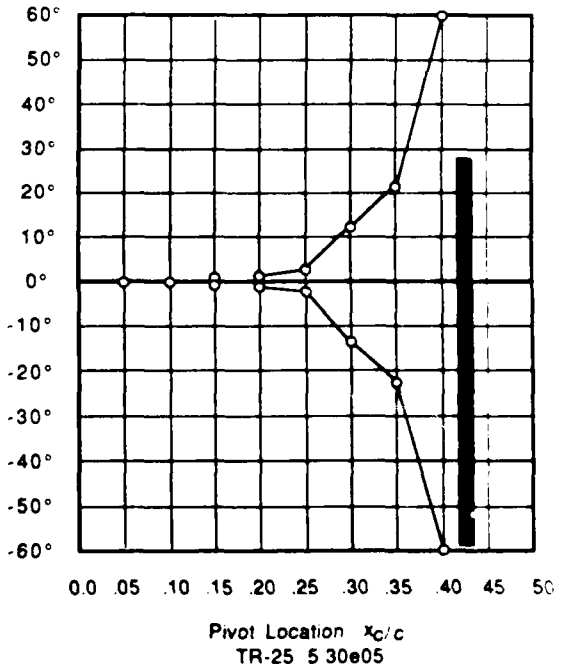

Fig. 7.19 continued

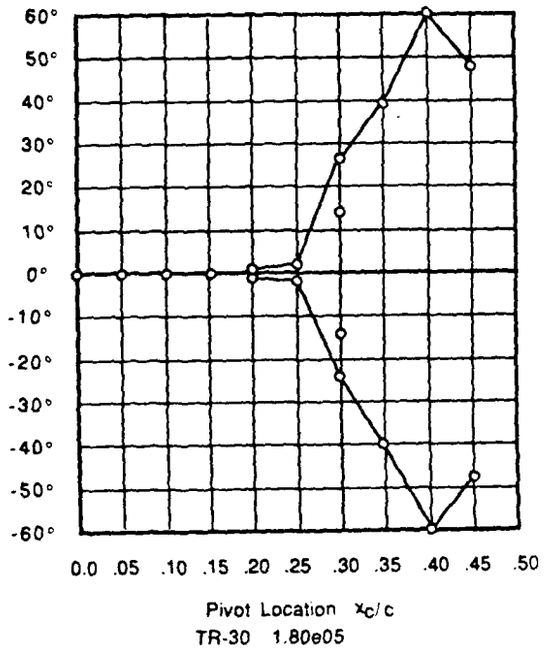

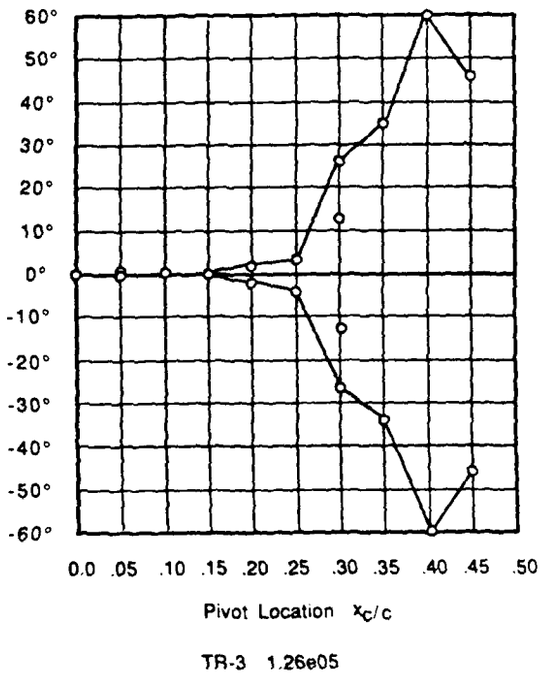

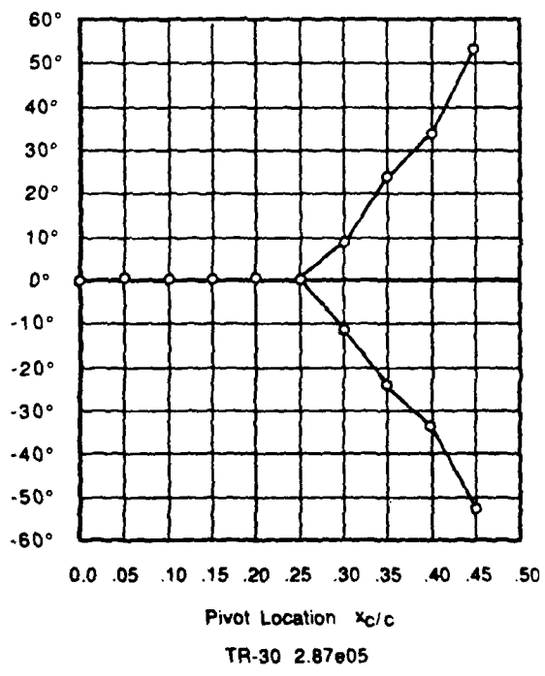

Fig. 7.20 JfS 62M TR-30 yaw stability

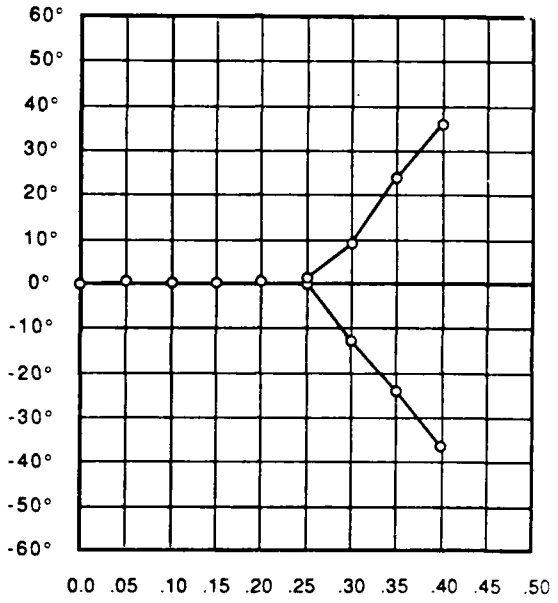

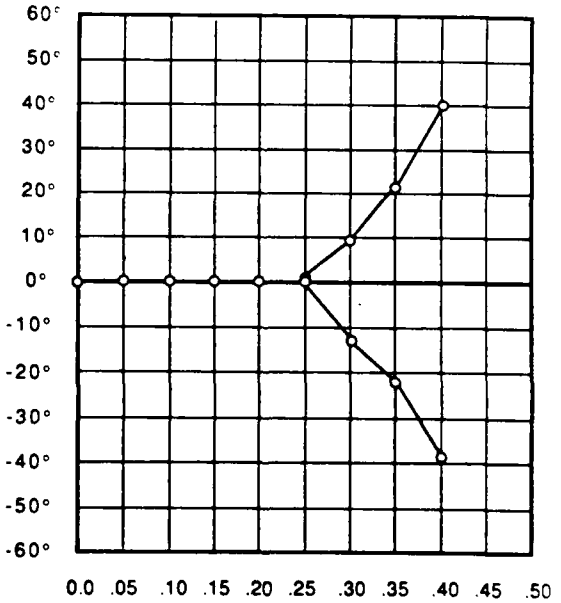

Fig. 7.20 continued

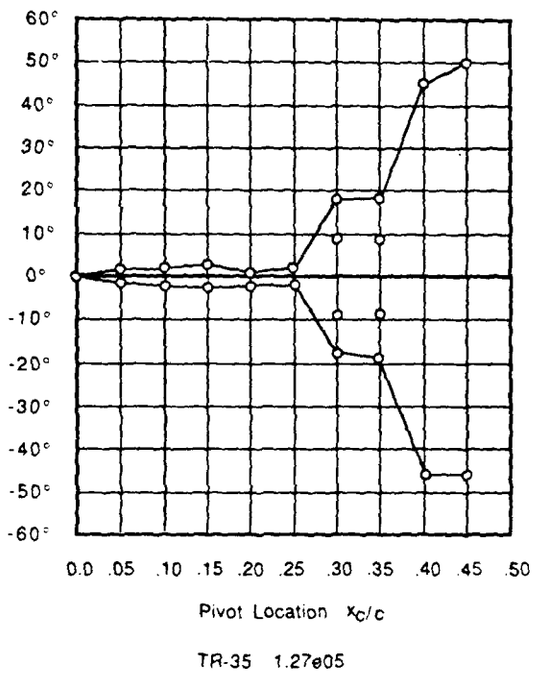

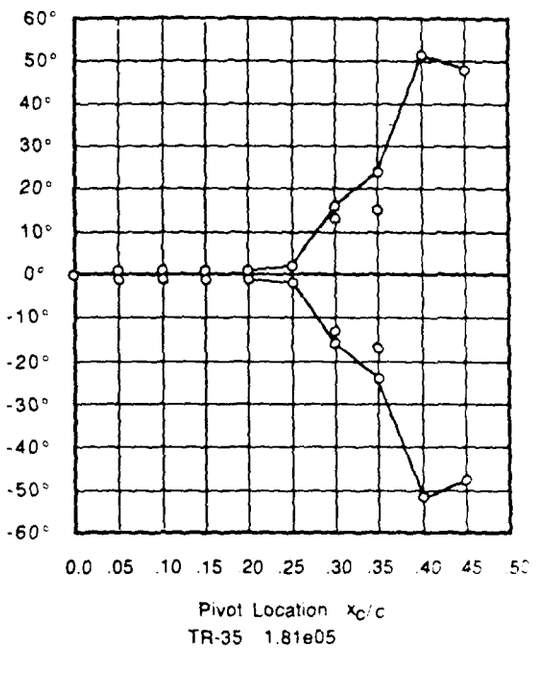

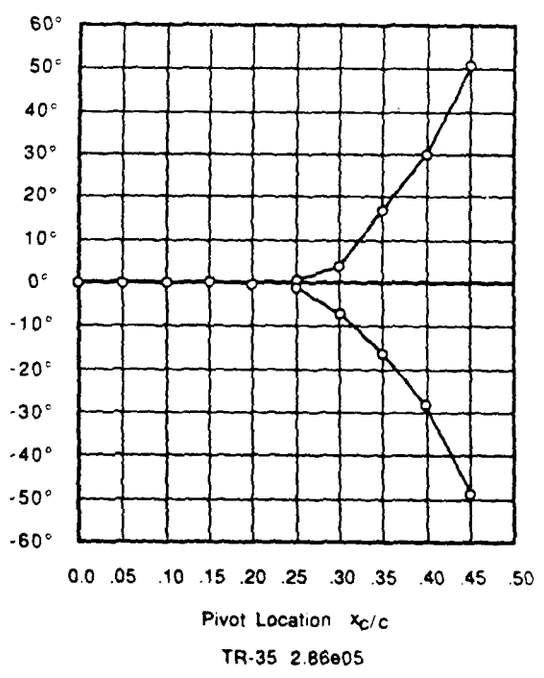

Fig. 7.21 JfS 62M TR-35 yaw stability

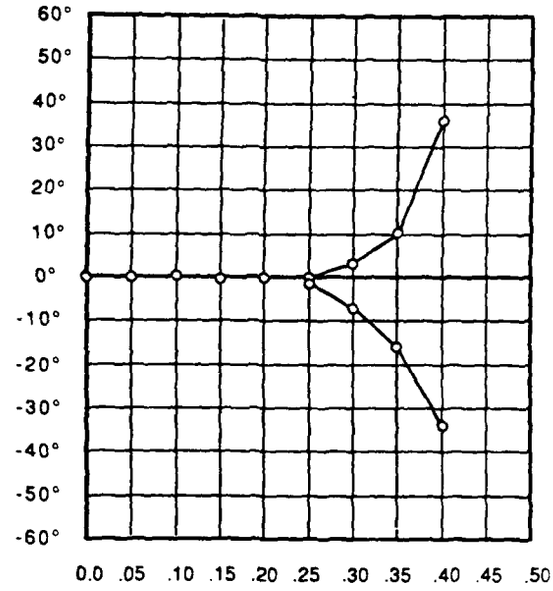

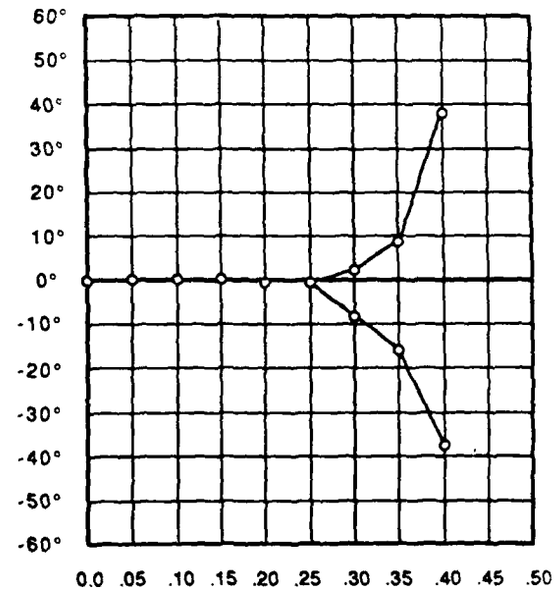

Fig. 7.21 continued

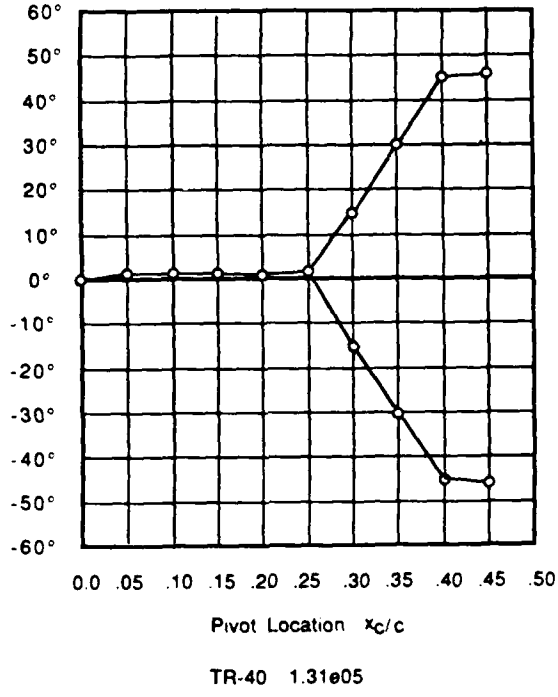

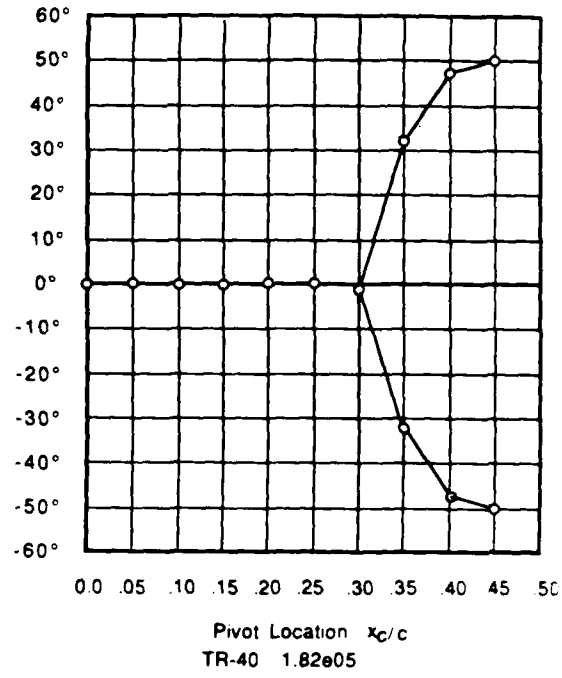

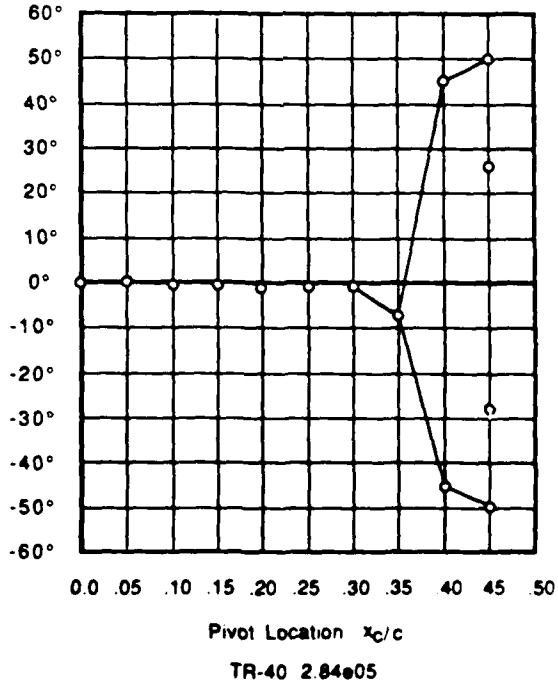

Fig. 7.22 JfS 62M TR-40 yaw stability

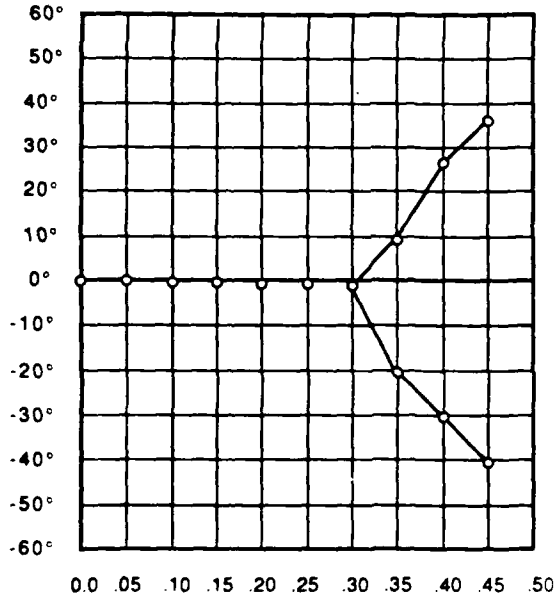

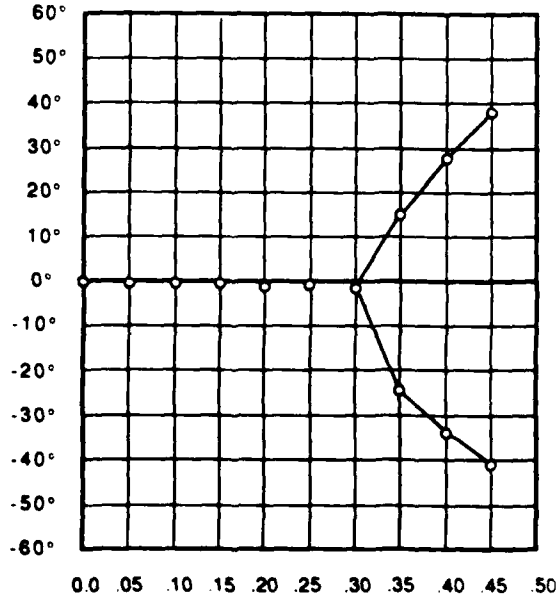

Fig. 7.22 continued

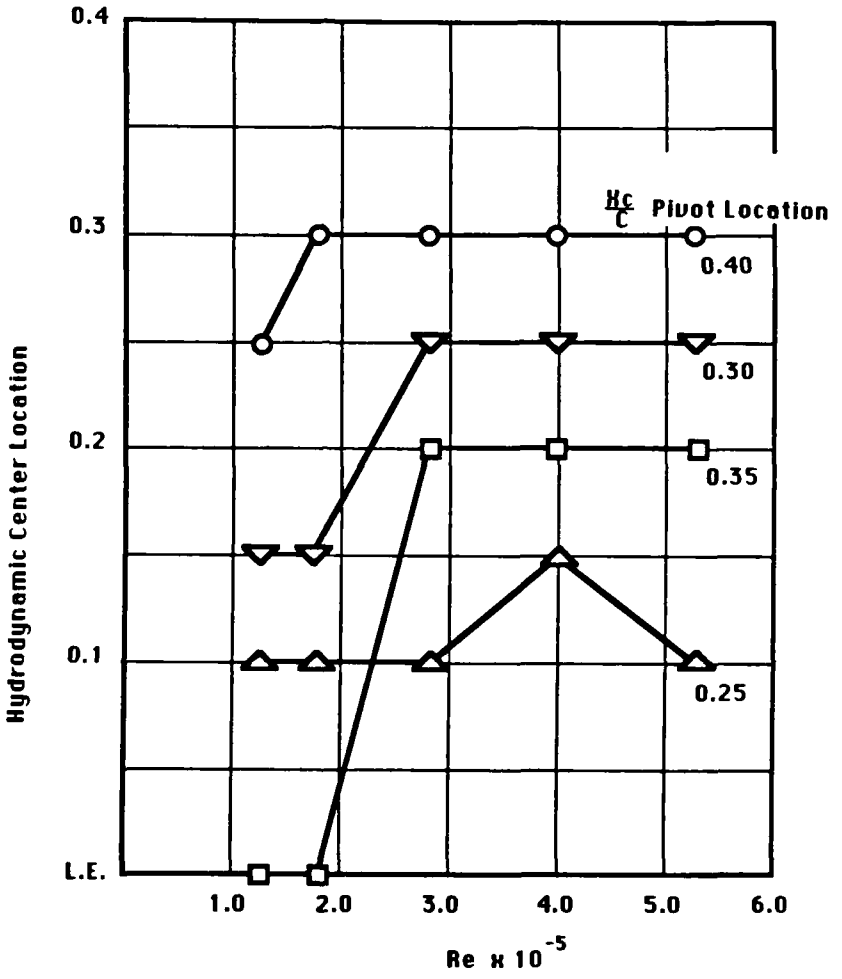

Fig. 7.23 Hydrodynamic center location

4. the fairing must be dynamically stable throughout the Reynold s number range encountered during towing.

Calkins and Gray [2] showed that the JFS61 and 62M -40 sections demonstrated weathervane stability for hydrodynamic center positions up to 0.3 chord.

Yaw equilibrium may be described by four stability states:

1. Stable - the fairing model assumes an equilibrium position at zero yaw angle, and will return to this position if displaced slightly. The most rearward pivot position for the state is the hydrodynamic center.

2. Neutrally Stable - the fairing model will assume a position of equilibrium over a range of yaw angles. Beyond this range, the model is stable about the range boundary angles.

3. Static Instability - the fairing model will assume a position of equilibrium at a positive or negative yaw angle, with no stable or neutrally stable position within this range.

4. Dynamic Instability - the fairing model will experience periodic yaw oscillations over a range of angles.

7.4.2. Experimental Stability States

Yaw equilibrium angle boundaries for each of the four thickness/chord ratio models are shown as a function of pivot location in Figures 7.19 through 7.22. Data for discrete Reynolds numbers of 1.27, 1.81, 2.84, 4.0, and 5.3 x 10^5 are shown. Each figure is intended to portray the makeup of the four stability states as defined previously. In addition, the stable yaw equilibrium angle position boundary also is shown. These charts may be used to determine the position of the hydrodynamic center as the most aft position for which state 1 stability was exhibited.

From a design standpoint, it is the position of the hydrodynamic center location that is the most important to the designer, although the existence and location of the stability states 2, 3, and 4, are of interest. It is assumed that the designer would chose the position of the mechanical pivot to be at some position forward of the hydrodynamic center. The exact position would be determined from consideration from the size and materials of the actual fairing under design, as the hydrodynamic restoring moment must be balanced against the moment required to overcome the rotational friction of the mechanical pivot.

While the purpose of the wind tunnel test was to determine the position of the hydrodynamic center, because of the technique used to determine this variable, the wind tunnel model also experienced the effects of friction. The models were designed to be mechanically rotated at five percent chord increments measured from the leading edge. Brass pins were inserted in the top and the bottom of the model to a depth of between one-half to one inch. Mechanical friction on this pin at the top and bottom of the model, including mechanical friction about 3/4-inch diameter washer had to be overcome by the hydrodynamic forces. Care was taken to reduce this friction to a small a level

as possible by reducing the size of the mechanical friction area to a minimum and by coating the surface with petroleum jelly. It was expected that the frictional resistance of mechanical rotation friction would be most predominant at the lower Reynolds number where the hydrodynamic moments were lowest.

The position of the hydrodynamic center, the neutral point position for which state 1 stability existed, is shown in Figure 7.23 as a function of Reynolds number for each of the four models. Of immediate interest is the general trend of a rearward movement of the hydrodynamic center location with increasing thickness to chord ratio. The thinest model, t/c = 0.25, showed a hydrodynamic center location at about 10 percent of the chord. The 30 percent thickness to chord model showed a rearward movement, with a location of 25 percent at the higher Reynolds numbers. It should be noted that a position of 25 percent is the classic location of the hydrodynamic center. The 35 percent thickness to chord ratio model showed an anomoulous behavior with no stable position at the two lowest Reynolds numbers increasing to a position at 20 percent at the three highest Reynolds numbers. This seemed to lie between the results for the 25 percent and 30 percent models.

It is felt that there may have been mechanical problems with the mechanical pivot pins such that an unduly large amount of friction existed. The 40 percent thickness to chord model shows a position at 30 percent of the chord over most of the Reynolds number range. This agrees with the results of Calkins and Gray [1].

9.0 CONCLUSIONS

Unfortunately, the Phase (2) tests were not entirely successful. Two discrepancies were found.

1) The tunnel configuration of the balance mounted horizontal models were found to have end plate/model junction horseshoe vortices which precluded two-dimensional flow. Thus the drag, lift and pitching moment measurements could not be made.

2) There is disagreement between the wake momentum blockage/drag coefficients for the JFS 62M TR-40 section measured with the differential pressure transducer in Phase (1), [1], on the manometer board. The drag coefficient values for Phase (1) were substantially higher as were the blockage values.

3) However, the results of the boundary layer and the hydrodynamic center location studies were successful. The results for the JFS 62M TR-40 section agreed with those from the Phase (1) study.

10.0 RECOMMENDATIONS

1) The presence of the model/endwall horseshoe vortices disrupted the 2-D flow over the model span. The investigators were consequently unable to measure the 2-D characteristics of the models as planned. For future research, it is felt that following modifications to the model configuration will allow true 2-D flow over the model. Extensions will be added to the current models that allow balance measurements in the 2-D flow region of the model with the endwall losses restricted to the junction of the extensions with the wind tunnel wall, Fig. 10.1.

2) A new data acquisition and differential pressure system should be developed based on the 32 bit Macintosh microcomputer. This will considerably speed the acquisition and reduction of the wake measurement data. The wake measurement data can be compared with the balance results and rechecked against the Phase (1) data.

Venturi Windtunnel Cross-section
Recommended Horizontal Model Configuration

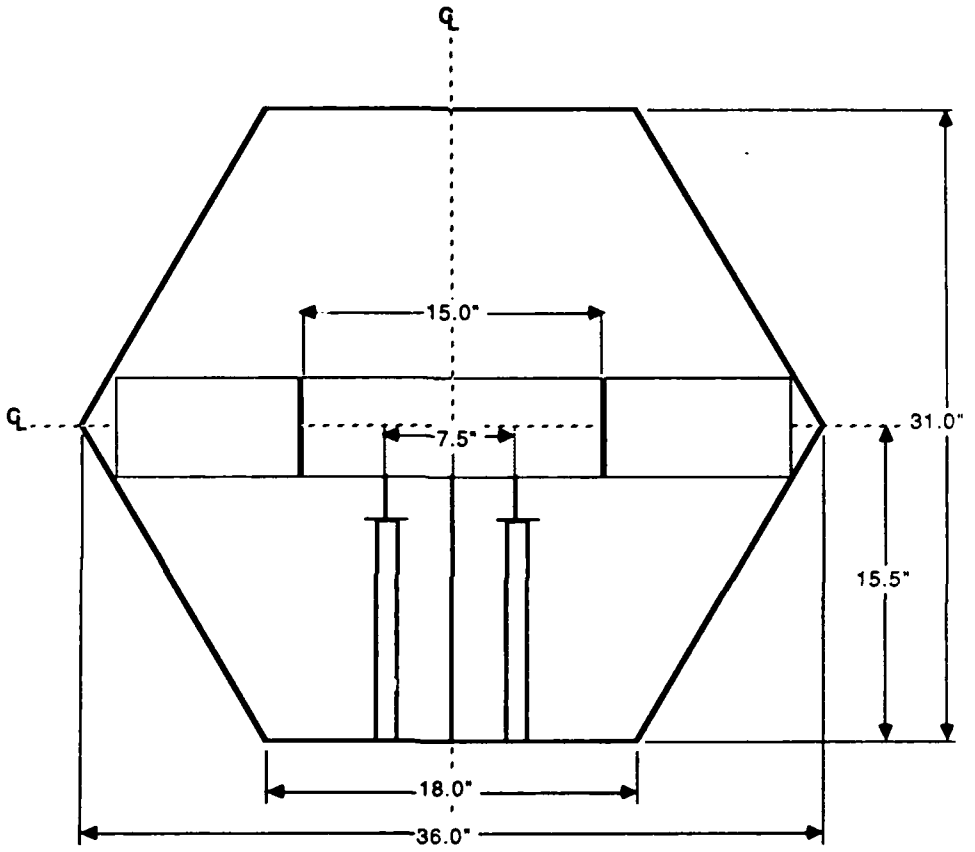

Fig. 10.1 Venturi Windtunnel cross-section recommended horizontal model configuration

REFERENCES

1. Calkins, D.E. and Gray, D.L., "An Experimental Investigation of the Two-dimensional Hydrodynamic Characteristics of Bluff Symmetrical Fairing Sections," University of Washington, March 1984.

2. Hoerner, S.F., Fluid Dynamic Drag, published by Author, Midland Park, New Jersey, 1958.

3. Thieme, H., "Design of Ship Rudders," ("Zur Formgebung von Shiffsrudern"), translated by E.N. Labouvie, Department of the Navy, Trans. 321, November 1965.

4. Pope, A., and Harper, J.J., Low-Speed Wind Tunnel Testing, Wiley, New York, 1966.

5. Boulil, S., "Minimizing Uncertainties in Airfoid Drag Determination Using Momentum Defect Integral Measurement," University of Washington.

6. Maskew, B., "Program POT2D, 2-Dimensional Potential Flow Program," Analytical Methods, In Redmond, Washington, 1981.

7. Shaw, R.J., Sotos, R.G. and Solano, F.R., "An Experimental Investigation of Airfoil Icing Characteristics," NASA Lewis Research Center, AIAA Paper No. 82-283, 1982.

8. Fritsch, F.N. and Carlson, R.E., "Piecewise Cubic Interpolation Methods," Lawrence Livermore Laboratory Report, UCRL-81230, November 1978.

9. Shabaka, I.M.M.A., and Bradshaw, P., "Turbulent Flow Measurements in an Idealized Wing/Body Junction," AIAA Journal, Vol. 19, No. 2, February 1981, pp. 131-132.

10. Mehta, R.D., Shabaka, I.M.M.A., and Bradhshaw, P., "Symposium on Numerical and Physical Aspects of Aerodynamic Flows," Cal. State Univ., January 1981.

11. Kuchemann, D., "The Aerodynamic Design of Aircraft," Pergamon Press, 1970, pp. 274-275.

12. Baker, C.J., "The Turbulent Horseshoe Vortex," Journal of Wind Engineering and Industrial Aerodynamics, 6, 1980, pp. 9-13.

13. Belik, L., "The Secondary Flow about Circular Cylinders Mounted Normal to a Flat Plate," Aeronautical Quarterly, 1982.

14. Han, L.S., Ma, C., and Rapp, J.R., "The Endwall Influence on Heat Transter from a Single Cylinder (The Horseshoe Vortex Effect)," International Gas Turbine Congress, 1983, Tokyo.

15. Johnston, J., "The Turbulent Boundary Layer at a Plane of Symmetry in a Three-Dimensional Flow," Transactions of the ASME, September 1960, pp. 622-628.

16. Barber, T.J., "An Investigation of Strut-Wall Intersection Losses," Journal of Aircraft, Vol. 15, No. 10, pp. 676-681.

17. Henderson, J.F., "Some Towing Problems With Faired Cables," Ocean Engineering, Vol. 5, pp. 105-125, 1978.

5,77